Technical University of Denmark

DTU

Wind tunnel test of the RISØ-1 airfoil

Fuglsang, Peter; Antoniou, I.; Bak, Christian; Aagaard Madsen , Helge

Publication date:
1998

Document Version
Publisher's PDF, also known as Version of record

[Link back to DTU Orbit](#)

DTU Library
Technical Information Center of Denmark

Wind Tunnel Test of the RISØ-1 Airfoil

Peter Fuglsang, Ioannis Antoniou, Christian Bak, Helge Aa. Madsen

Abstract

Wind tunnel tests with approximately 2d flow were carried out for the RISØ-1 airfoil in the VELUX open jet wind tunnel. The airfoil section was mounted in a test stand equipped with end plates to retain 2d flow conditions. The stand was then inserted into the tunnel test section. The Reynolds number was 1.6 million, the chord of the airfoil model 0.6 m and the span 1.9 m. Pressure distribution measurements provided the aerodynamic load coefficients and wake rake pressure measurements provided the total drag coefficient. Wind tunnel corrections were applied for streamline curvature and down-wash. Steady inflow measurements showed that the airfoil behaved well with a well defined maximum lift coefficient of 1.3, a minimum drag of 0.0075, and a smooth stall region. Comparisons with numerical predictions from the EllipSys2D Navier-Stokes code showed good agreement among the calculated and measured lift and drag coefficients. Leading edge roughness devices were found to reduce the maximum lift coefficient by 15% to 1.1 and to increase the drag coefficient at low incidence. Dynamic inflow measurements with the airfoil in pitching motion were carried out to study the hysteresis effects on the aerodynamic coefficients. The lift coefficient hysteresis loops at high incidence had smooth shapes and did not show leading edge separation. Steady inflow measurements at high angles of attack showed that the airfoil flow was stationary and did not indicate double stall.

Contents

Nomenclature

c	[m]	Airfoil chord
h	[m]	Jet height
k		Reduced frequency
Δp	[Pa/m]	Pressure loss
p	[Pa]	Static pressure
p_o	[Pa]	Total pressure head
q	[Pa]	Dynamic pressure
s		Airfoil surface coordinate
t	[s]	Pitch motion time
x		Chordwise coordinate
y		Wake rake vertical coordinate, airfoil vertical coordinate
A	[°]	Pitch motion amplitude
C_D		Drag coefficient
C_L		Lift coefficient
C_M		Moment coefficient
C_N		Normal force coefficient
C_P		Airfoil pressure coefficient
C_T		Tangential force coefficient
Re		Reynolds number
T	[°C]	Air temperature
V	[m/s]	Velocity
α	[rad] [°]	Angle of attack
ε		Speed-up factor
ρ	[kg/m^3]	Air density
ω	[rad/s]	Pitch motion angular velocity

Subscripts
1-3	Pitot tube measurement
a	Airfoil section measurement
j	Jet outlet measurement
m	Mean value
min	Minimum value
max	Maximum value
p	Pressure measurement
t	Measured value (uncorrected)
w	Wake rake measurement
∞	Reference for normalisation of airfoil forces

1 Introduction

This report concerns 2d wind tunnel tests of the Risø-1 airfoil. The tests were carried out in the VELUX wind tunnel, which has an open test section. Pressure distribution measurements were taken on the airfoil section together with wake rake pressure measurements. The testing facility is described in detail in Fuglsang *et al.*, 1998 [1].

The Risø-1 airfoil was designed in 1993 and is intended for use on the outer part of blades for stall regulated wind turbines with a Reynolds number between one and two million, Madsen, 1994 [2] . A moderate maximum lift coefficient of 1.3 is obtained with a fast movement of the suction side transition point towards the leading edge just before stall. This causes trailing edge separation on a considerable part of the airfoil. Below stall the pressure distribution on the suction side of the airfoil is rooftop like and a laminar boundary layer is obtained on 50 – 60% of the suction side. The airfoil was used for the blades of a 12.6 m rotor tested in 1993-1994, Antoniou, 1994 [3]. Measurements showed good and stable stalling characteristics of the rotor and the power production was satisfactory. The airfoil test section was manufactured and instrumented by Risø.

The testing program included:
- Steady and quasi-steady inflow measurements where mean values were obtained for the airfoil load coefficients. The angle of attack was changed in steps of 2° and a 20 s interval during which a time series was obtained for each angle of attack. Alternatively the angle of attack was changed continuously at a rate around 0.3°/s with continuos measurement.
- Long duration time series were measured to reveal the nature of the flow in the post stall region.
- Dynamic inflow was measured with the airfoil in pitching motion at amplitudes around ±2° and reduced frequencies around 0.1. The hysteresis effects on the aerodynamic coefficients were derived.

All tests were carried out at Reynolds number 1.6 million. The incidence range was between -5° and 30°.

The airfoil was tested with:
- Smooth surface.
- Roughness applied to the leading edge to simulate the change in performance of the aerodynamic coefficients from dirt and dust deposits.

2   Experimental set-up

The experimental set-up is briefly described whereas a more complete description can be found in Fuglsang *et al.*, 1998 [1].

2.1 Testing facility

The VELUX wind tunnel is of the closed return type with an open test section of 7.5×7.5 m and a length of 10.5 m, Figure 2-1. The cross section of the jet blowing into the test section is 3.4×3.4 m. The maximum flow velocity is 45 m/s.
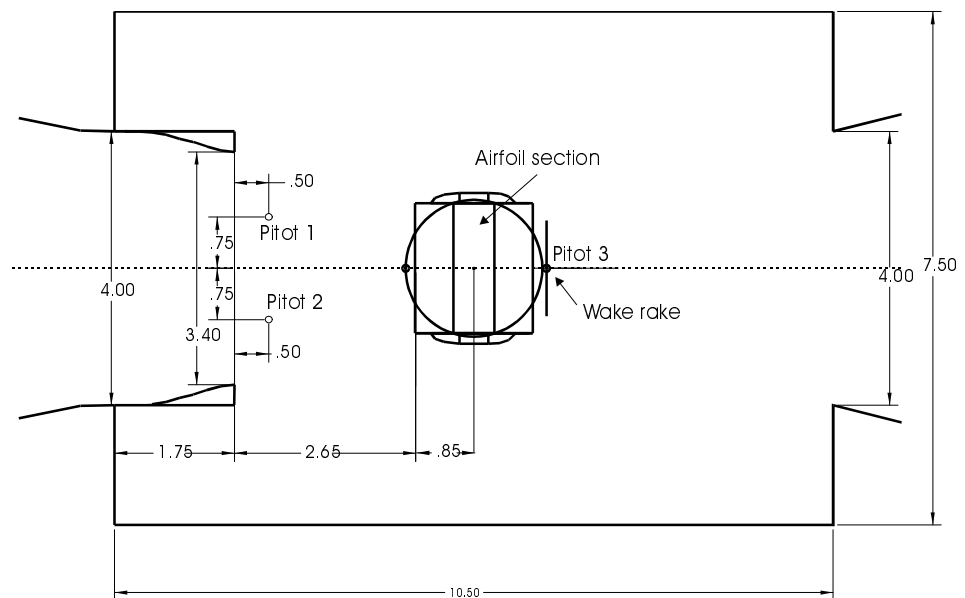

Figure 2-1 The wind tunnel test section with the test stand seen in a top view.

A test stand was built for 2d airfoil testing, Figure 2-2. The test stand was inserted in the tunnel test section. The airfoil section with a span of 1.9 m was mounted 1.7 m from the tunnel floor and 3.2 m from the nozzle outlet. The chord was 0.6 m. To limit 3d effects endplates were fixed to the stand at the ends of the airfoil section.

Three Pitot tubes measured static and total pressure at different locations in the test section, Figure 2-1. These Pitot tubes were also used to measure the wind tunnel reference pressures.

Steady measurements at continuously varying angles of attack were possible. Dynamic inflow measurements were also possible by pitching the airfoil section in a cyclic motion at different reduced frequencies until $k = 0.15$ and amplitudes between $\pm 2° < A < \pm 5°$, see section 2.4.
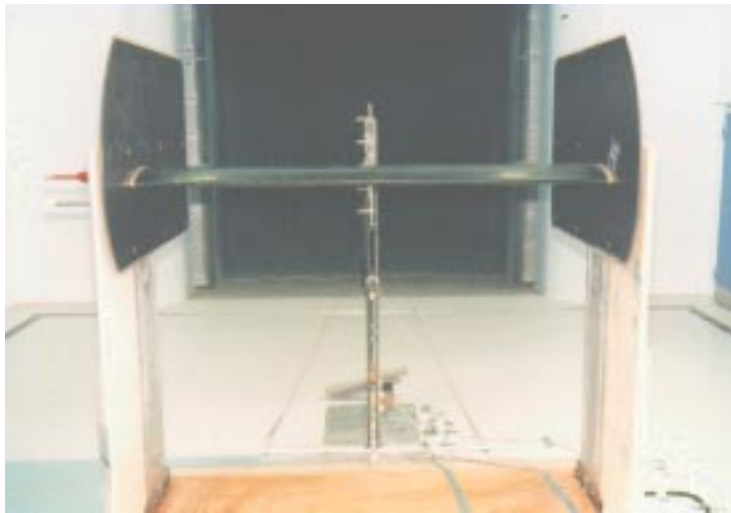
Figure 2-2 The test section with the test stand and the wake rake downstream of the airfoil section.

The wake rake consisted of 54 total pressure probes and five static tubes. The vertical span was 0.456 m, Figure 2-3. The distance between the airfoil trailing edge and the wake rake was 0.7 chords and the middle of the wake rake was placed at the height of the trailing edge at 0° incidence. The rake was not traversed in the horizontal or the vertical directions.
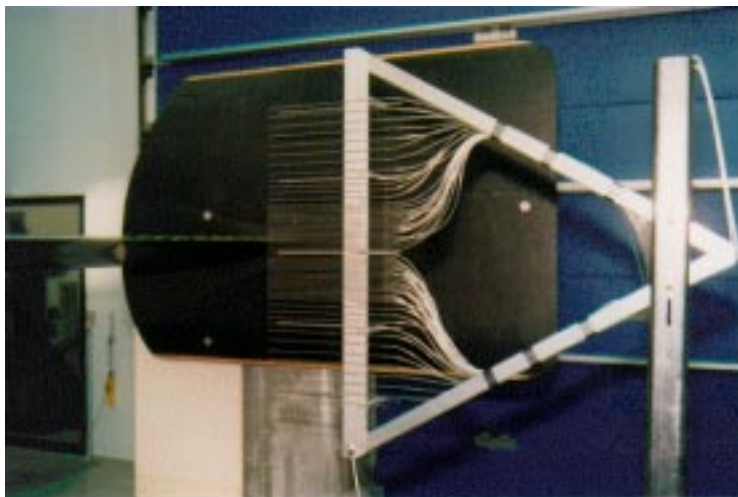

Figure 2-3 The wake rake seen from the side in front of an endplate.

The HyScan 2000 data acquisition system from Scanivalve Corp. was used. Two ZOC33 pressure-scanning modules recorded the pressure signals. For the airfoil surface pressures, 40 1 psi and 24 2.5 psi sensors were used. For the wake rake and for pitot tubes, 10˝ H_2O sensors were used. The ZOC module for the airfoil pressures was mounted on the test stand side. The tubes were lead from the airfoil section through a hollow axis and all tubes had equal length. The wake rake and pitot tubes ZOC module was placed at the floor below the wake rake. A ZOCEIM16 module was used for the acquisition of the electrical signals.

At normal operation, a total of 134 signals were measured by the data acquisition system:

- 64 airfoil surface static pressures, $p_a(s)$
- 5 wake rake static pressures, $p_w(y)$
- 53 wake rake total pressures, $p_{ow}(y)$
- 3 Pitot tube static pressures, p_{1-3}
- 3 Pitot tube total pressures, p_{o1-3}
- Angle of attack, α
- Air temperature, T
- Air density, ρ
- 2 strain gauges for recording shaft bending
- Electric motor frequency

2.2 Wind tunnel boundary corrections

Wind tunnel corrections should be applied for streamline curvature and down-wash. Horizontal buoyancy, solid and wake blockages could on the other hand be neglected because of the open jet, which is free to expand, Ray and Pope, 1984 [4].

Streamline curvature is introduced to the flow, especially in the case of open test sections, when solid walls do not bound the jet and the flow is free to diverge downstream of the airfoil section. The curvature of the flow induces drag and changes the effective angle of attack over the airfoil. In the case of the VELUX tunnel, the presence of the floor close to the jet bottom boundary will influence streamline curvature and introduce uncertainty on the wind tunnel corrections. This influence was assumed to be negligible.

Down-wash is introduced to the flow when the jet dimensions exceed the airfoil section span. The airfoil section corresponds to a finite wing and trailing vortices appear at the ends of the span although reduced by the endplates. The trailing vorticity induces a down-wash velocity in the case a of positive lift coefficient. The angle of attack is reduced and additional drag is induced.

Both down-wash and streamline curvature result in a change in the angle of attack due to the induction of a velocity normal to the flow direction and the airfoil section. It is assumed in this case that down-wash is insignificant compared with streamline curvature because of the presence of endplates.

For the correction of streamline curvature, the method of Brooks and Marcolini, 1984 [5] was used.

The corrected free flow angle of attack, α, is found from:

$$\alpha = \alpha_t - \frac{\sqrt{3\sigma}}{\pi} C_L - \frac{2\sigma}{\pi} C_L - \frac{\sigma}{\pi} (4C_{Mt}) \; [rad]$$
(2-1)

Where

$$\sigma = \frac{\pi^2}{48} \cdot \left(\frac{c}{h}\right)^2$$
(2-2)

The drag coefficient, C_D, is calculated from:

$$(2-3)$$

$$C_D = C_{Dt} + \left[-\frac{\sqrt{3\sigma}}{\pi} C_L \right] C_L$$

The moment coefficient, C_M, is obtained:

$$C_M = C_{Mt} - \frac{\sigma}{2} C_L \qquad (2-4)$$

For details see Fuglsang *et al.*, 1998 [1].

2.3 Wind tunnel flow conditions

The turbulence intensity at the test section inlet is 1%. Between the inlet and the airfoil section, there is a speed-up of, $\varepsilon_{j-a} = 6.9\%$, and a pressure drop of $\Delta p_{j-a} = 15$ Pa/m, Fuglsang *et al.,* 1998 [1].

The wind tunnel references for static, p_∞ and total pressures, $p_{o\infty}$ were derived from Pitot 1 measurements, Figure 2-1. The speed-up between Pitot 1 and the airfoil section, $\varepsilon_{1-\infty} = 5.9\%$ and the pressure drop between Pitot 1 and the airfoil section, $\Delta p_{1-\infty} = 15$ Pa/m were determined in Fuglsang *et al.,* 1998 [1] and they are taken into account at the calculation of p_∞ and $p_{o\infty}$.

2.4 Calculation methods

The airfoil pressure coefficient, $C_p(s)$, along the airfoil surface, s, is calculated from:

$$C_p(s) = \frac{p_a(s) - p_\infty}{q_\infty} \qquad (2-5)$$

Where

$$q_\infty = p_{o\infty} - p_\infty \qquad (2-6)$$

The normal force coefficient, C_N, and the tangential force coefficient, C_T, are found from integration of $C_P(s)$. The airfoil lift coefficient, C_L, and drag coefficient, C_D are found by resolving C_N and C_T perpendicular to and parallel with the oncoming flow:

$$C_L = \cos(\alpha)C_N + \sin(\alpha)C_T$$

$$(2-7)$$

$$C_D = -\cos(\alpha)C_T + \sin(\alpha)C_N$$

The moment coefficient, C_M, is found from integration of $C_P(s)$ at $x/c = 0.25$.

The total airfoil drag is the sum of skin friction and pressure drag. By assuming a control surface, which surrounds the airfoil section, the total drag can be

calculated from the balance of the momentum flux entering the control surface in front of the airfoil and the momentum flux exiting the control surface behind the airfoil section. The momentum profile entering is assumed uniform and is calculated from the wind tunnel reference pressures while the momentum profile exiting is calculated from the pressures measured by the wake rake.

Assuming that the flow is 2d, the total wake drag coefficient, C_{Dw}, is calculated from Rae and Pope, 1984 [4]:

$$C_{Dw} = \frac{2}{c} \int_{y_{min}}^{y_{max}} \sqrt{\frac{p_o(y) - p(y)}{q_\infty}} \cdot \left(1 - \sqrt{\frac{p_o(y) - p(y)}{q_\infty}}\right) dy \qquad (2\text{-}8)$$

In the analysis of dynamic loads, while the airfoil is in pitching motion, the pitching motion is defined:

$$\alpha = A\sin(\omega t) + \alpha_m \qquad (2\text{-}9)$$

The pitching motion is related to the reduced frequency:

$$k = \frac{\omega c}{2V_\infty} \qquad (2\text{-}10)$$

3 The airfoil section

The span of the airfoil section was 1.9 m and the chord was 0.60 m. Risø manufactured and instrumented the model.

3.1 Pressure taps

The airfoil section was equipped with 56 pressure taps of 0.5 mm inner diameter. The pressure taps were placed along the chord at the centreline in a staggered alignment to minimise disturbances from upstream taps. The taps were drilled directly through the model surface and into metal pressure tubes lying parallel to the model surface. Flexible plastic tubes were connected to the metal tubes and they were lead outside of the model through a hollow axis. The pressure tap at the trailing edge was out of order.

The chordwise location of the pressure taps can be seen in Figure 3-1 where the actual model coordinates are compared with the theoretical coordinates from Madsen, 1994 [2]. The overall agreement is good in the leading edge region but the thickness of the model was increased compared with the theoretical coordinates. At the trailing edge, the model thickness was also increased compared with the theoretical coordinates because of manufacturing reasons.

3.2 Aerodynamic devices

In some of the measurement campaigns, leading edge roughness was simulated by sandpaper mounted on the airfoil suction side from the leading edge to 5% chord. The type NAXOS, grain size 120, width 32 mm was used. Leading edge roughness was not applied to the pressure side.
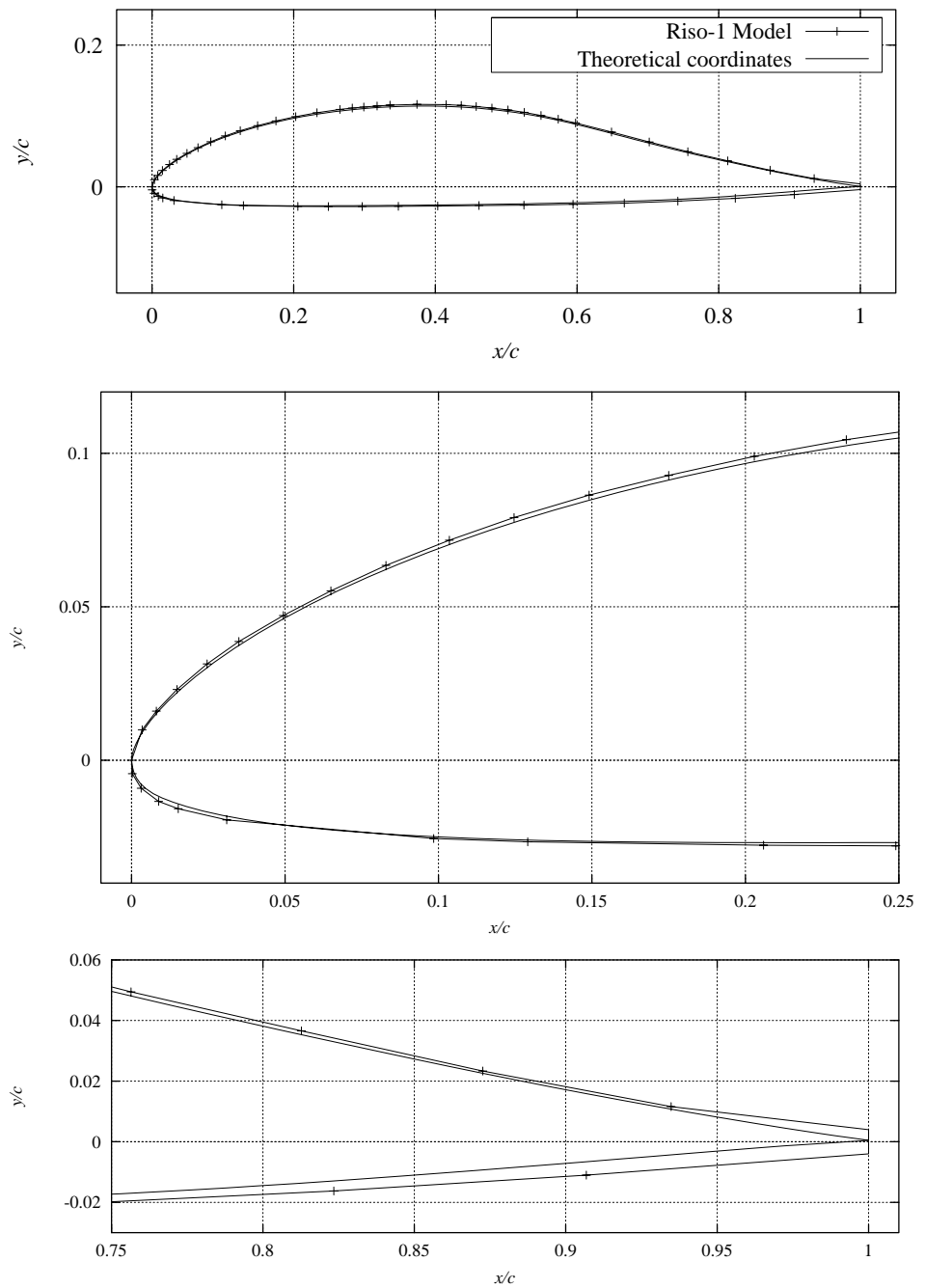
Figure 3-1 The actual model coordinates compared with the theoretical coordinates. Each cross symbol corresponds to a pressure tap. The leading edge and the trailing edge regions are shown enlarged.

4 Smooth leading edge

This chapter reports results from steady inflow measurements with smooth leading edge. The different types of measurements are described in Appendix A1. The Reynolds number was in all measurements $Re = 1.6\times10^6$. All shown results were corrected for wind tunnel effects and the aerodynamic forces were referenced to the wind tunnel free stream flow by use of Pitot 1 taking into account corrections for speed-up and pressure loss.

The measurements were compared with numerical predictions. The XFOIL code based on a panel method with a viscous boundary layer formulation was used, following Madsen and Fillipone, 1995 [6]. Free transition was modelled with the e^n method, Drela, 1989 [7]. The Ellipsys2D Navier-Stokes code, Sørensen, 1995 [8], with the k-ω turbulence model, Menter, 1993 [9], was used for turbulent flow predictions. Free transition was modelled using the Michel transition criteria, Michel, 1952 [10]. All predictions were carried out on the airfoil section corresponding to the theoretical coordinates from Madsen, 1994 [2] with a sharp trailing edge.

4.1 Pressure distributions

Figure 4-1 shows the measured C_P distributions for different angles of attack. Each C_P distribution was deduced from a 20 s time series, sampled at 5 Hz. Since the pressure tap at the trailing edge was out of order the trailing edge C_P was set to zero for all angles of attack. There is some scatter in the C_P values at the suction side of the leading edge region until $x/c = 0.18$, caused by either uncertainty of the calibration or small irregularities of the surface or the pressure taps. The pressure sensor at $x/c = 0.18$ appeared to be out of order since there was a kink in the pressure at all angles of attack.

At all angles of attack the leading edge stagnation point is captured well with small variations due to the limited resolution offered by the pressure taps along the chord. The overall quality of the C_P distributions is sufficient for calculation of aerodynamic load coefficients.

Up to $\alpha = 6.7°$ there is a rooftop like C_P distribution at the suction side extending to $x/c = 0.5$ with a smooth pressure recovery toward the trailing edge. The C_P on the pressure side decreases linearly starting from the stagnation point to the trailing edge. Above $\alpha = 6.7°$ trailing edge separation occurs, which extends to $x/c = 0.5$. At the same time a C_P peak gradually builds up at the leading edge. The sudden separation ensures a well defined C_{Lmax}.

The C_P peak is present up to $\alpha = 25.0°$. As a result suction and lift is maintained and C_L varies smoothly in the post stall region after C_{Lmax} is reached. At $\alpha = 25.0°$ the flow is separated from the leading edge.
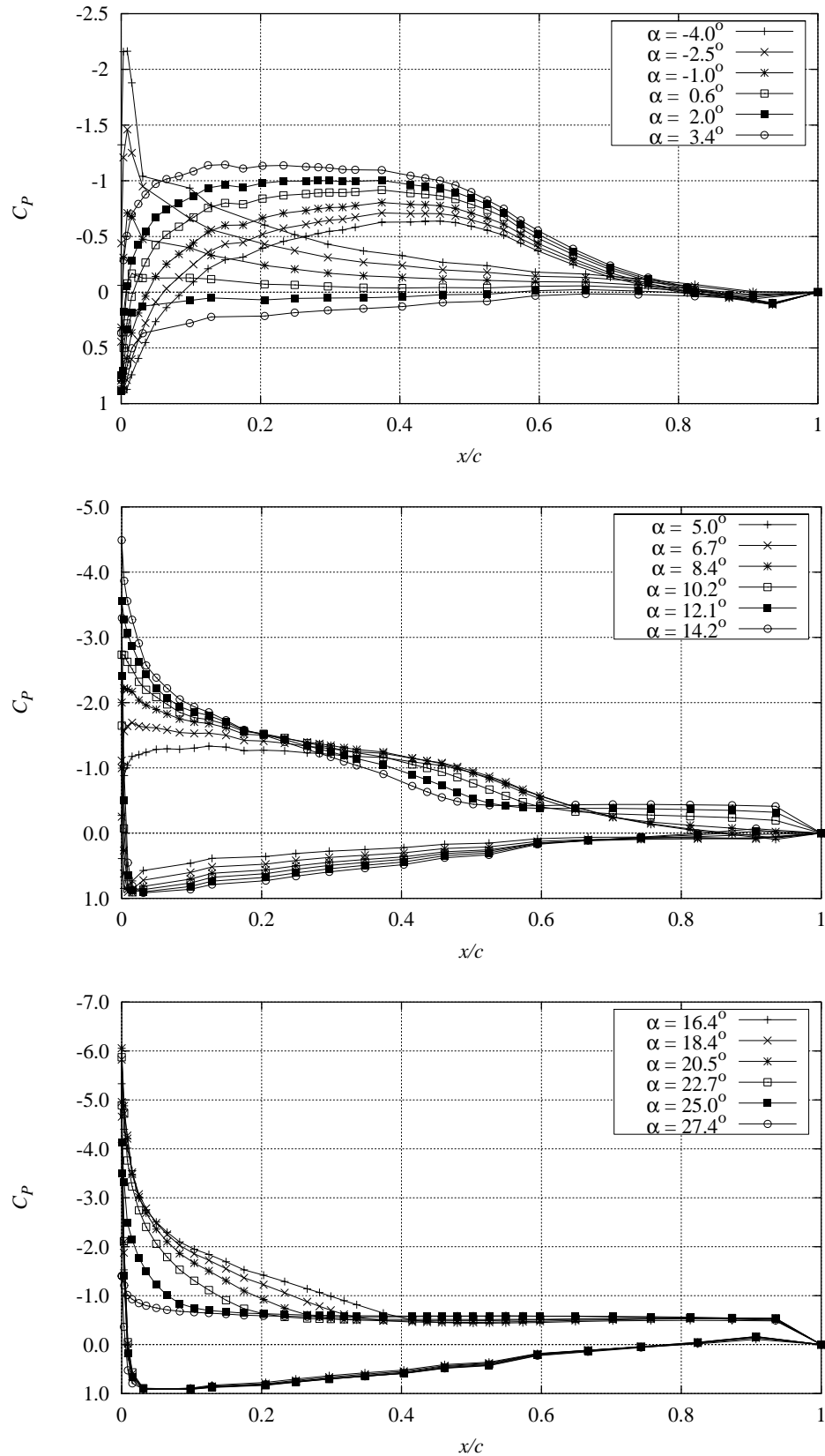
Figure 4-1 Measured C_P distributions at different angles of attack, Re = 1.6×10^{6} (RISØ-1STEP 221196V1).

Figure 4-2 shows the measured C_P distribution at $\alpha = 0.6°$ compared with an Ellipsys2D free transition flow prediction and an XFOIL free transition prediction. The overall agreement with both predictions is good. At the leading edge suction side, the measured C_P is slightly lower compared with the predictions, but the rooftop region and the pressure recovery region are in good agreement.

XFOIL and EllipSys2D both predict the transition point after the rooftop region. XFOIL furthermore predicts a laminar separation bubble in connection with transition, which neither the measured C_P distribution nor the EllipSys2D predictions confirm. It is likely that the bubble is not present in the measurement because of the rather high turbulence level of 1%.

At the leading edge pressure side, there is a small difference between the measurement and the predictions. The small differences between measurements and predictions are caused by either a small difference in the actual angle of attack from uncertainty on the wind tunnel corrections or by small surface differences between the model and the theoretical coordinates at the leading edge. At the trailing edge there are also some discrepancy between computations and measurements. However, as noted above the trailing edge pressure tap measurement was arbitrarily set to zero. Furthermore, the computations were made for a sharp trailing edge.
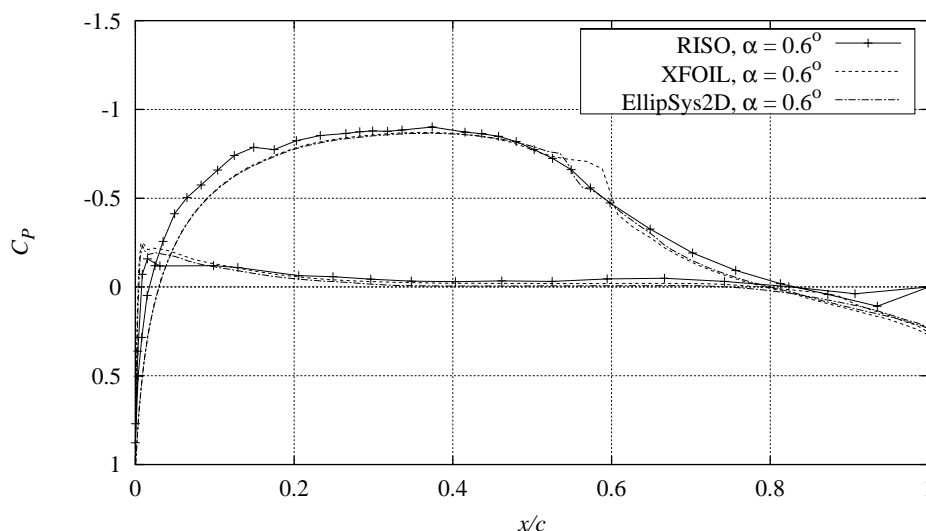

Figure 4-2 Measured C_P distribution compared with XFOIL and Ellipsys2D predictions, Re = 1.6×10⁶, α = 0.6° (RISØ-1STEP 221196V1).

Figure 4-3 shows the measured C_P distribution at $\alpha = 5.0°$ compared with EllipSys2D and XFOIL predictions with free transition. Except for some scatter at the suction side leading edge region in the measurement, the agreement is good. XFOIL again predicts a laminar separation bubble in the transition region, which is neither found in the EllipSys2D prediction nor in the measurement. The measured C_P on the pressure side is slightly irregular compared with the predictions, but the deviations are small and do not influence the calculation of aerodynamic forces.
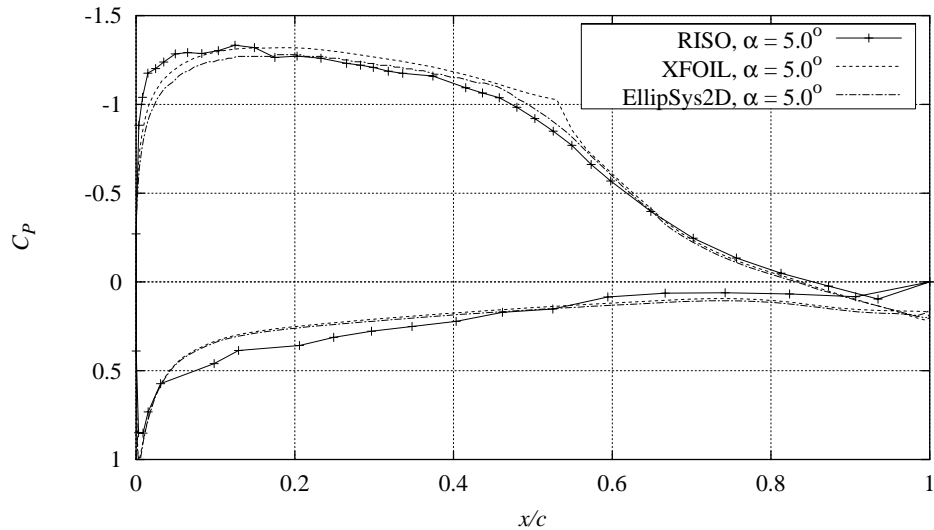
Figure 4-3 Measured C_P distribution compared with XFOIL and Ellipsys2D predictions, $Re = 1.6\times10^6$, $\alpha = 5.0°$ (RISØ-1STEP 221196V1).

Figure 4-4 shows the measured C_P distribution at $\alpha = 10.2°$ compared with XFOIL and EllipSys2D predictions with free transition. EllipSys2D is in better agreement with the measurement, compared with XFOIL. Both predictions show slightly lower C_P at the suction side compared with the measurement. XFOIL furthermore shows the transition point around $x/c = 0.08$. The flow is separated from the trailing edge and the measurement shows the separation point around $x/c = 0.65$, whereas the predictions show separation around $x/c = 0.7$. The transition point location, the free flow turbulence and the magnitude of the suction peak influence the location of the separation point. The pressure side C_P is in good agreement despite minor scatter.
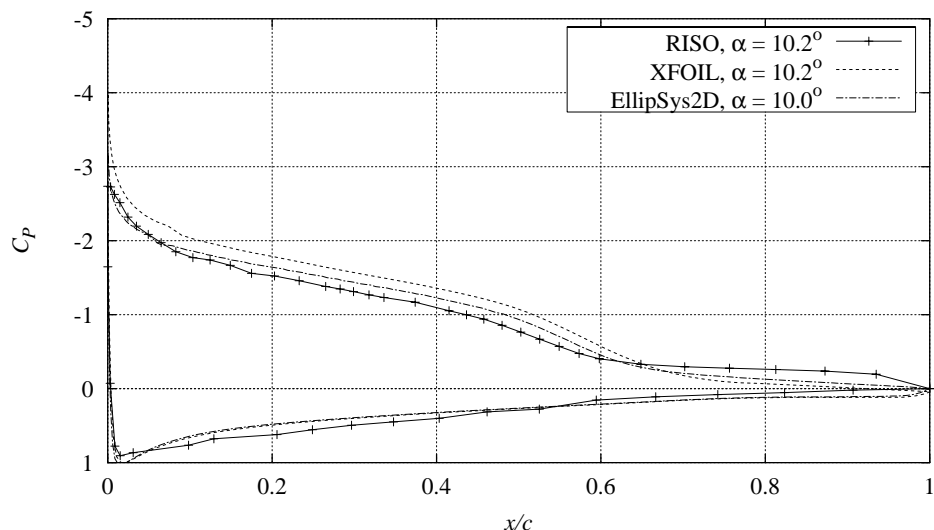

Figure 4-4 Measured C_P distribution compared with XFOIL and Ellipsys2D predictions, $Re = 1.6\times10^6$, $\alpha = 10.2°$ (RISØ-1STEP 221196V1).

Figure 4-5 and Figure 4-6 show the measured C_P distribution at $\alpha = 14.2°$ and $\alpha = 18.4°$ respectively compared with XFOIL and EllipSys2D predictions. The comparisons show the same trends as in Figure 4-4 with $\alpha = 10.2°$, but the predicted transition points moved toward the leading edge.

At α = 18.4°, XFOIL differs from EllipSys2D and the measurement in the suction side leading edge region, where XFOIL overestimates the suction peak, which results in subsequent lower C_P toward the separation point. However, the separation points are located similar and the pressure side C_P is in good agreement.
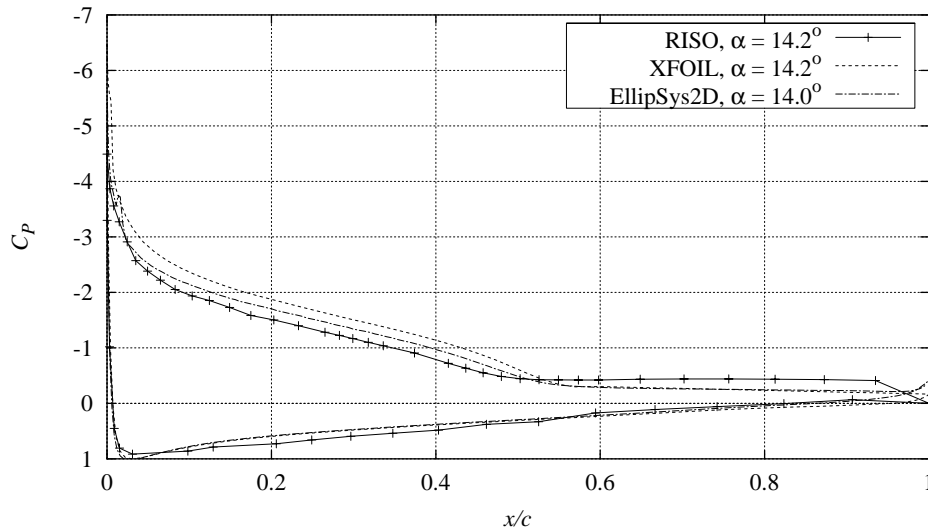

Figure 4-5 Measured C_P distribution compared with XFOIL and Ellipsys2D predictions, Re = 1.6×10^6, α = 14.2° (RISØ-1STEP 221196V1).
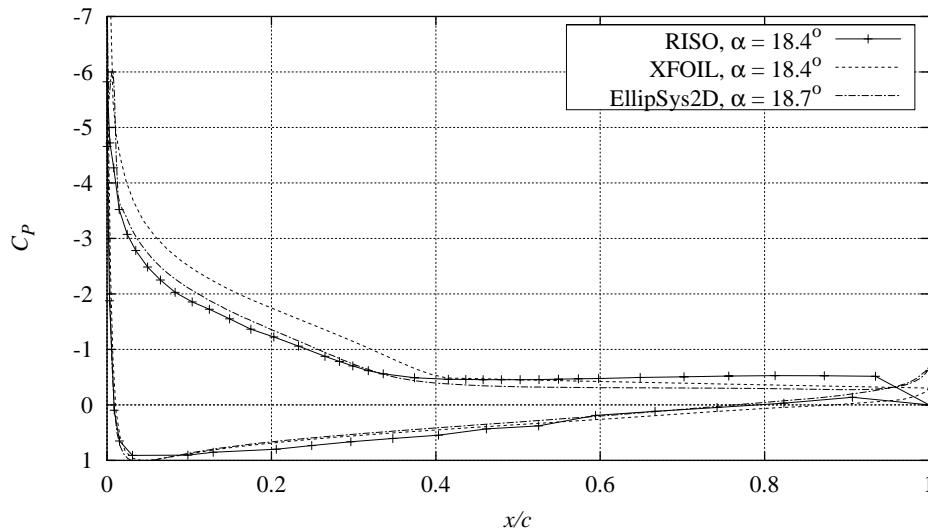

Figure 4-6 Measured C_P distribution compared with XFOIL and Ellipsys2D predictions, Re = 1.6×10^6, α = 18.4° (RISØ-1STEP 221196V1).

4.2 Load coefficients

Figure 4-7 shows the measured C_L curve. Each measurement point is the average value of a 20 s time series sampled with 5 Hz taken with constant α. The angle of zero lift is α = -3.2° and C_{Lmax} is 1.3. The lift curve slope is $dC_L/d\alpha$ = 0.115. In accordance with the results presented in Section 4.1, the C_L

curve starts to bend off at $\alpha = 6°$ and C_{Lmax} occurs at $\alpha = 14.5°$. The post stall region is smooth.

The measurement is compared with an XFOIL prediction with free transition and EllipSys2D predictions with free transition and turbulent flow respectively.

The agreement between measurements and all predictions is very good at angles of attack below $\alpha = 3°$. Between $\alpha = 3°$ and $\alpha = 8°$, the XFOIL prediction is unstable, which is probably caused by the presence of the laminar bubble on the suction side at the transition point, Figure 4-3, and by the Stratford like pressure recovery region. XFOIL overestimates C_{Lmax}, because of too low suction side C_P, Figure 4-5 and Figure 4-6.

The agreement between measurements and Ellipsys2D with free transition is very good at all angles of attack. There is only a minor deviation at $\alpha = 3°$ and C_{Lmax} is only slightly overestimated. The EllipSys2D prediction with turbulent flow is quite similar to the free transition prediction except for a slightly lower C_L curve slope. However, C_{Lmax} is equal in both predictions, which indicates insensitivity of C_{Lmax} to the location of the transition point, which means that C_{Lmax} (in theory) is insensitive to leading edge roughness.
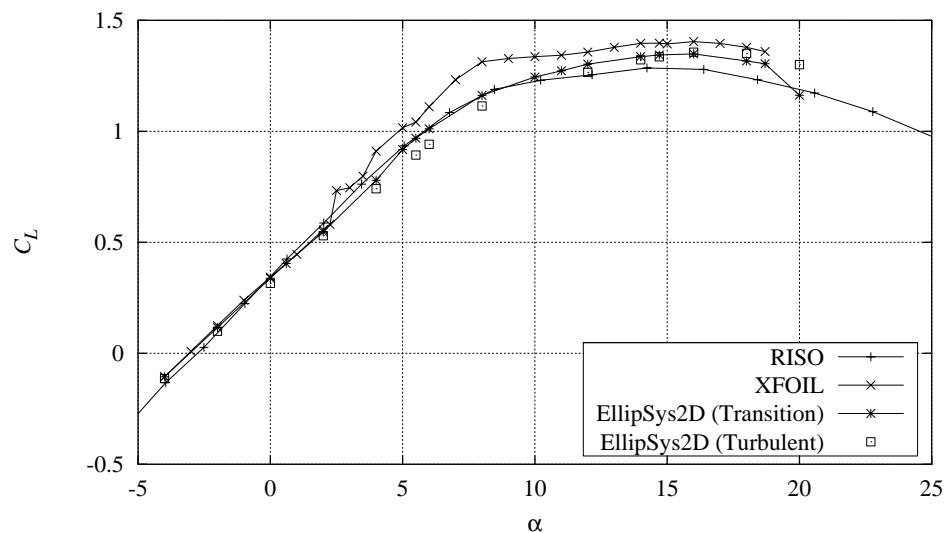

Figure 4-7 Measured C_L curve compared with XFOIL predictions (free transition) and Ellipsys2D predictions (turbulent flow and free transition), Re = 1.6×10⁶ (RISØ-1STEP 221196V1).

Figure 4-8 shows the measured C_D curve. At low angles of attack, C_D was calculated from the wake rake. After the flow starts to separate, C_D was calculated as pressure drag from the C_P distribution and drag from skin friction was neglected, which is a valid assumption at high angles of attack. Minimum drag was measured to $C_{Dmin} = 0.0075$ at $\alpha = 2°$. The low drag area was measured between $\alpha = 1°$ and $\alpha = 4°$.

The measurement is compared with an XFOIL prediction with free transition and EllipSys2D predictions with free transition and with turbulent flow respectively. The XFOIL and EllipSys2D free transition predictions were in good agreement with the measurement at angles of attack below $\alpha = 8°$, while the EllipSys2D turbulent flow prediction overestimates C_D at low angles of attack. Taking into consideration the uncertainty related to the wake rake drag

calculations, the agreement between measurements and predictions is considered good. The drag rise related to stall appears around 8° and the drag rise slope is slightly underestimated by the predictions.
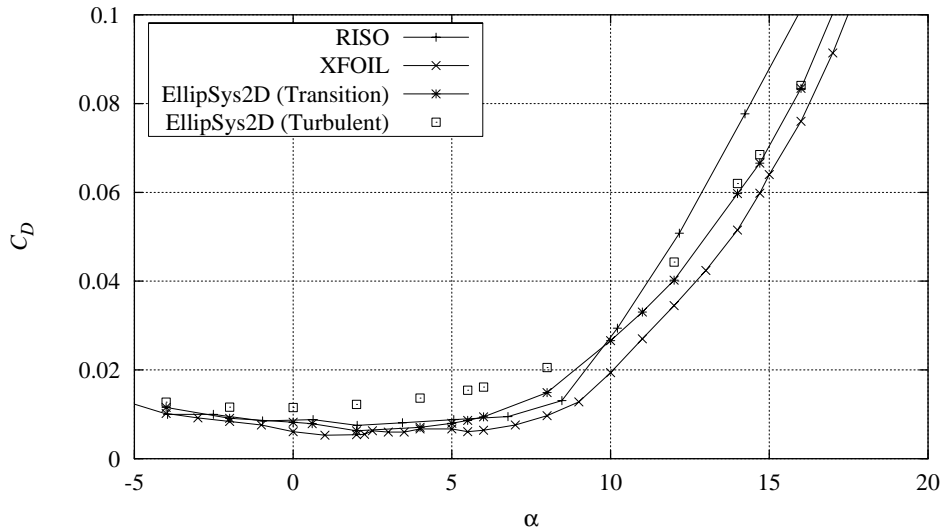

Figure 4-8 Measured C_D curve compared with XFOIL predictions (free transition) and Ellipsys2D predictions (turbulent flow and free transition), Re = 1.6×10^6 (RISØ-1STEP 221196V1).

Figure 4-9 shows the measured C_L-C_D curve compared with the numerical predictions. The low drag values are more clear in this plot and the low drag area for the measurement is between $C_L = 0.4$ and $C_L = 1.0$. Whereas the XFOIL prediction shows some scatter, the shape of the EllipSys2D free transition prediction is in good agreement with the measurement, with nearly identical minimum C_D and identical drag rise.
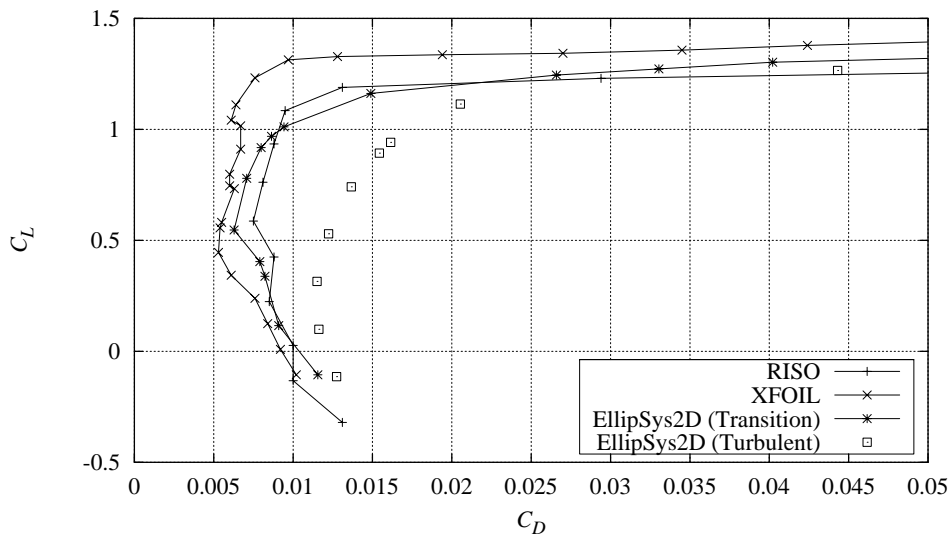

Figure 4-9 Measured C_L-C_D curve compared with XFOIL predictions (free transition) and Ellipsys2D predictions (turbulent flow and with free transition), Re = 1.6×10^6 (RISØ-1STEP 221196V1).

Figure 4-10 shows the measured C_M curve compared with the XFOIL prediction with free transition. The agreement is fair at angles of attack below $\alpha = 2°$. However, the scatter regions in the XFOIL prediction and C_M at higher angles of attack are not in agreement with the measurements.
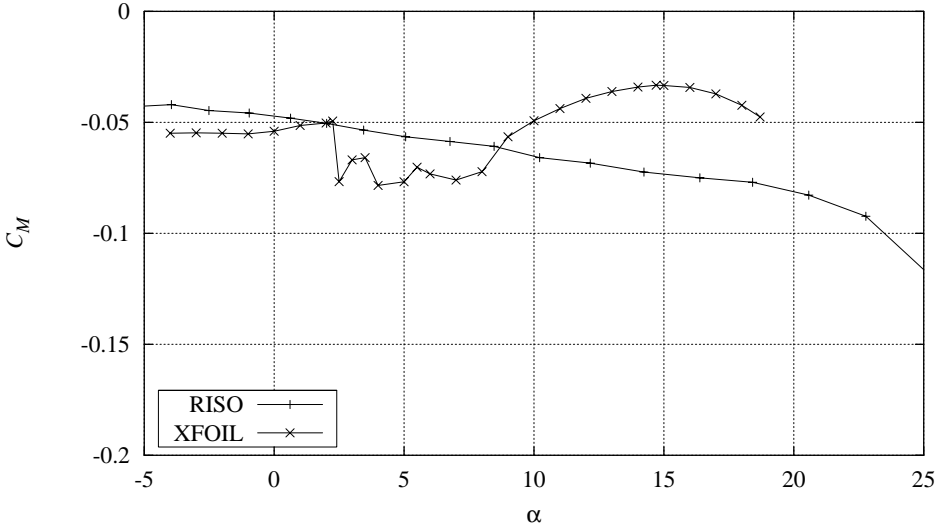

Figure 4-10 Measured C_M curve compared with XFOIL predictions (free transition), Re = 1.6×10⁶ (RISØ-1STEP 221196V1).

5 Leading edge roughness

In natural conditions, bugs and dirt often soil wind turbine blades at the leading edge and this reduces their aerodynamic performance. The sensitivity of the wind turbine power production to leading edge roughness (LER) is therefore important.

To investigate the impact on the aerodynamic performance, roughness was applied at the leading edge of the airfoil and its characteristics were measured under these conditions. The applied leading edge roughness was described in Section 3.2.

The measurements were compared with numerical predictions. In XFOIL predictions, leading edge roughness was simulated by fixing the transition point to $x/c = 0.01$ at the suction side and $x/c = 0.01$ at the pressure side. This results in turbulent flow over the entire airfoil. In EllipSys2D predictions with leading edge roughness, transition was not modelled and the flow was turbulent on the entire airfoil.

With transition at the leading edge, both predictions included the effect from early transition and the turbulent boundary layer. However, an eventual jump in boundary layer momentum thickness from the physical presence of leading edge roughness could not be included.

5.1 Pressure distributions

Figure 5-1 shows the measured C_P distribution at $\alpha = 0.4°$ with LER compared with a smooth leading edge flow measurement and XFOIL and EllipSys2D numerical predictions. Both measurement distributions are 1 s average values from quasi-steady measurement series with continuos change of the angle of attack at a rate around $0.3°/s$.

The agreement between the different measurements is good except for the small difference in angle of attack hence LER does not influence the C_P distribution for low angles of attack. The agreement with predictions is also good except for the small differences caused by the different angles of attack, used in the comparisons.
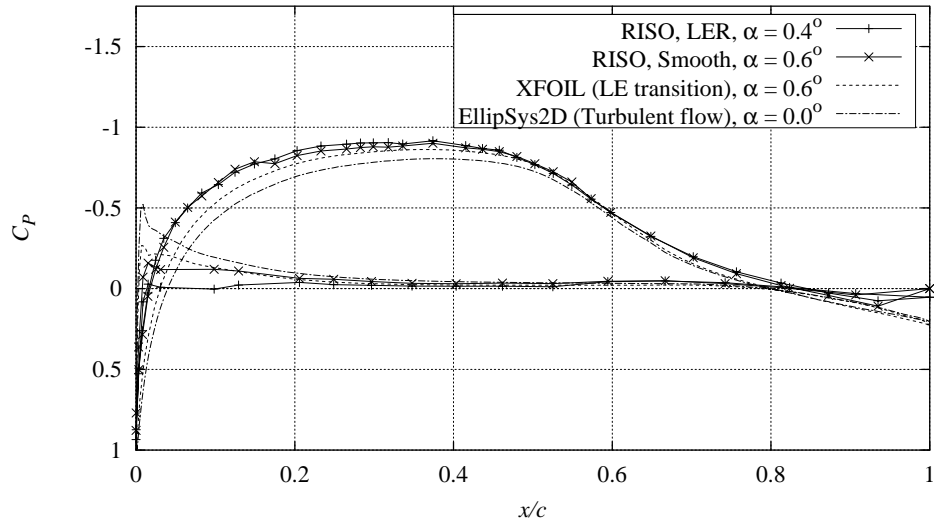
Figure 5-1 Measured C_P distribution for leading edge roughness compared with smooth measurement, XFOIL (LE transition) and EllipSys2D (Turbulent flow), Re = 1.6×10^6, α = 0.4°, (RISØ-1CONT 221196V1 and RISØ-1CONT 221196V2).

Figure 5-2 shows the measured C_P distribution at $\alpha = 10.2°$ with LER compared with a smooth leading edge flow measurement and XFOIL and EllipSys2D numerical predictions.

The C_P distribution for the LER measurement shows a reduced suction peak compared with the smooth leading edge measurement and the pressure is in general higher on the suction side. The separation point moved to $x/c = 0.55$ compared with $x/c = 0.7$ for smooth leading edge flow. The difference in the C_P distribution for LER will reduce C_L at the corresponding angles of attack and flow separation will appear at lower angles of attack.
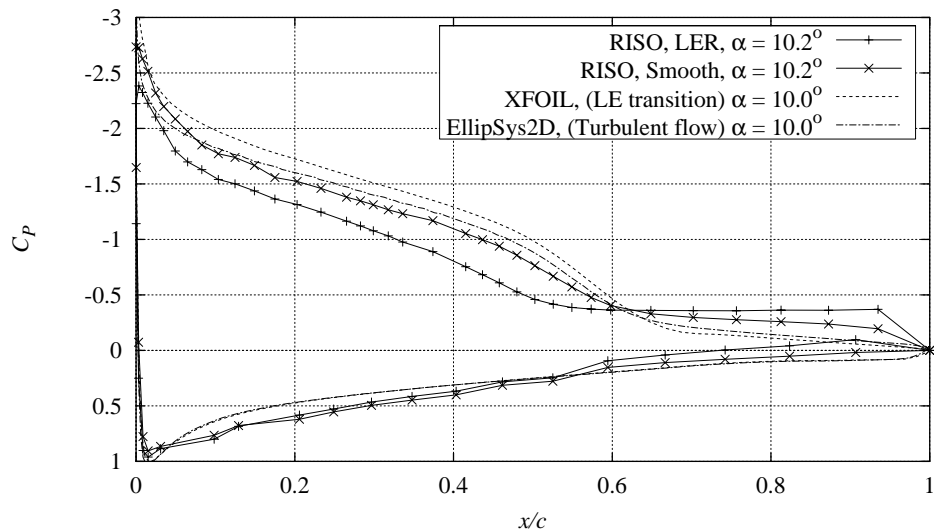

Figure 5-2 Measured C_P distribution for leading edge roughness compared with smooth measurement, XFOIL (LE transition) and EllipSys2D (Turbulent flow), Re = 1.6×10^6, α = 10.2°, (RISØ-1CONT 221196V1 and RISØ-1CONT 221196V2).

5.2 Load coefficients

Figure 5-3 shows the measured C_L curve for LER compared with smooth leading edge flow and numerical predictions. The measurements were performed with a continuous change of the angle of attack at a rate around 0.3°/s and the shown results were sorted in bins of the angle of attack of width 1°.

The slopes of the C_L curves are identical for both measurements at low angles of attack below $\alpha = 3°$. There are small irregularities in the measurements in this region, because of few available data points for the LER measurement. Separation starts at $\alpha = 3°$ and $C_{Lmax} = 1.1$ appears at $\alpha = 13°$. Compared with the smooth leading edge flow measurement, the shapes of the C_L curves are similar until high angles of attack.

The numerical predictions are nearly identical except for a small difference at C_{Lmax}. XFOIL predicts C_{Lmax} slightly higher compared with EllipSys2D as it was also the case for smooth flow, Section 4.2. The numerical predictions are not in good agreement with the LER measurement. There is a small difference in the angle of attack for zero C_L, the slope of the predicted C_L curve is in general too low and C_{Lmax} is predicted too high.

The numerical predictions show an airfoil flow where C_{Lmax} is insensitive to LER. Compared with smooth leading edge flow, the C_L curve slope is slightly reduced, but C_{Lmax} is retained around 1.3 –1.4. The measurements on the other hand show an airfoil flow where C_{Lmax} is reduced when LER is applied. From the comparison between LER measurements and the numerical predictions, it appears that the sand paper that was chosen to simulate leading edge roughness, Section 3.2, is not appropriate, since the roughness effects are too severe. The sand paper grain size of 120 is not too high in itself, but including the thickness of the sand paper, the influence on the measured flow is more severe than the effects from the movement of the transition point to the leading edge in the numerical predictions. In future measurements, well documented trip tape from the aviation research should be used in stead of sand paper.
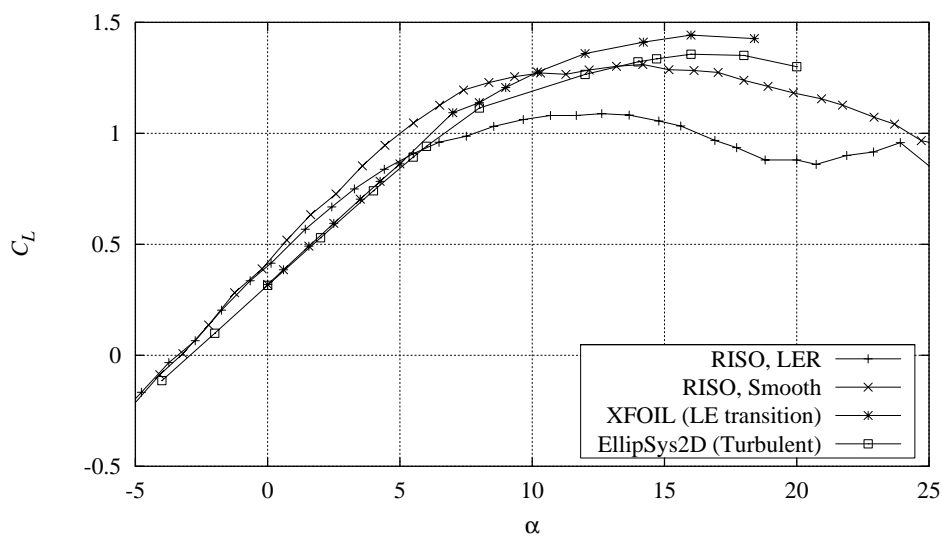

Figure 5-3 Measured C_L curve for leading edge roughness compared with smooth measurement, XFOIL (LE transition) and EllipSys2D (Turbulent flow), Re = 1.6×10⁶ (RISØ-1CONT 221196V1 and RISØ-1CONT 221196V2).

Figure 5-4 shows the measured C_D curve for LER compared with smooth leading edge flow and numerical predictions. Figure 5-5 shows the corresponding C_L-C_D curve. C_{Dmin} is clearly different for the two measurements and is increased from 0.0075 for smooth flow to 0.012 for the LER measurement. The drag rise appears at $\alpha = 7°$.

The numerical predictions are identical at low angles of attack and C_{Dmin} is in good agreement with the LER measurement. The drag rise appears slightly earlier for EllipSys2D than for XFOIL and EllipSys2D is in good agreement with the LER measurement. It appears that the sand paper simulates quite well the effects of LER on C_D, but this is most likely a coincidence.
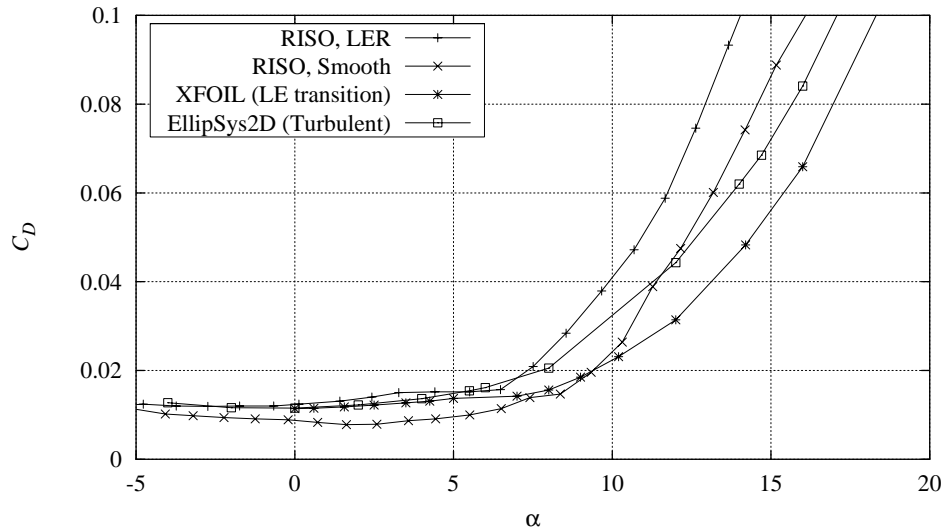

Figure 5-4 Measured C_D curve for leading edge roughness compared with smooth measurement, XFOIL (LE transition) and EllipSys2D (Turbulent flow), Re = 1.6×10⁶ (RISØ-1CONT 221196V1 and RISØ-1CONT 221196V2).
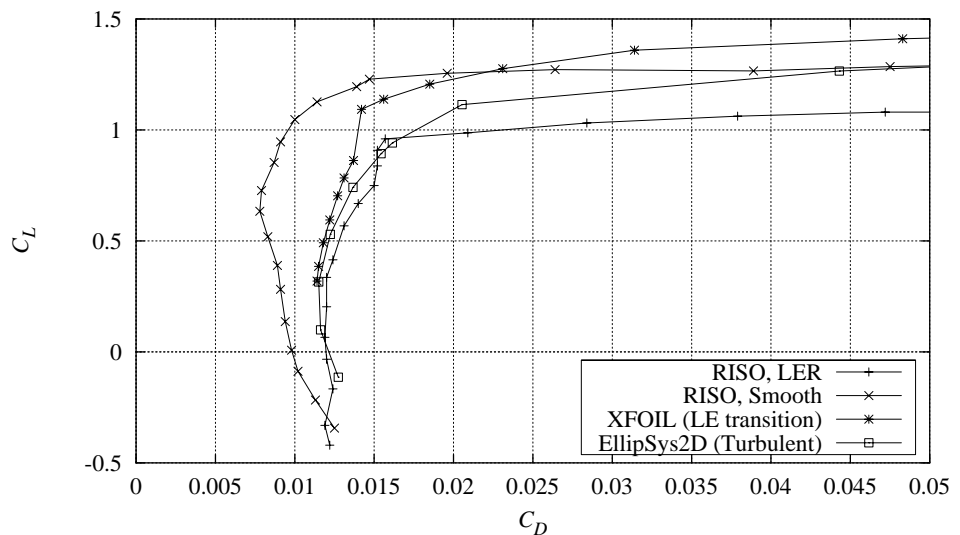

Figure 5-5 Measured C_L-C_D curve for leading edge roughness compared with smooth measurement, XFOIL (LE transition) and EllipSys2D (Turbulent flow), Re = 1.6×10⁶ (RISØ-1CONT 221196V1 and RISØ-1CONT 221196V2).

Figure 5-6 shows the measured C_M curve with LER compared with smooth leading edge flow and XFOIL numerical predictions. The difference between the measurements is in general low and there is good agreement between measurements and the XFOIL prediction at low angles of attack below $\alpha = 7°$. The XFOIL prediction deviates from the measurements above $\alpha = 7°$.
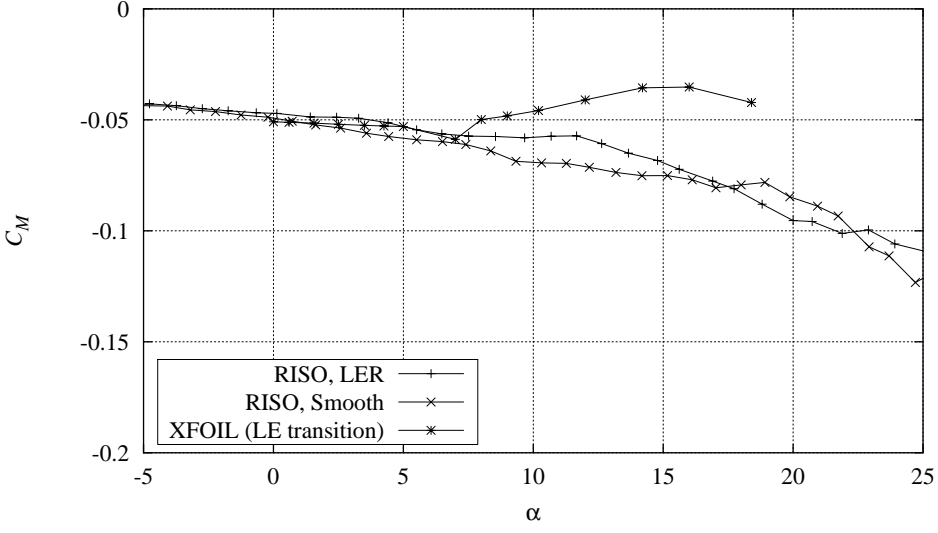

Figure 5-6 Measured C_M curve for leading edge roughness compared with smooth measurement and EllipSys2D (Turbulent flow), Re = 1.6×10⁶ (RISØ-1CONT 221196V1 and RISØ-1CONT 221196V2).

6 Dynamic stall

A measure of the airfoil dynamic behaviour is the response of the aerodynamic loads from a cyclic variation of the angle of attack. When the angle of attack is changed, the aerodynamic loading on the airfoil is altered and vortices are shed from the airfoil surface. The interaction of these vortices with the flow and the travel time along the airfoil causes a time lag between changes in the angle of attack and changes in the aerodynamic loading. This time lag combined with a time lag in the trailing edge separation is seen as hysteresis effects on the aerodynamic loads. Such measurements are important for the development of engineering models for dynamic stall.

While the airfoil was in pitching motion, the aerodynamic C_P distribution was measured and the momentary C_L, C_D and C_M were derived as a function of the angle of attack. Because of the unsteady flow, the wake rake could not be used to determine C_D and this was instead determined only as pressure drag from the C_P distribution. The pitching motion is related to the amplitude, A, and to the reduced frequency, k, defined in Section 2.5.

Measurements were performed at $k = 0.11$ and $k = 0.077$ with a geometric amplitude of $A_t = 2.0°$. Due to the non-linear wind tunnel corrections applied to the angle of attack, the nominal geometrical changes from the cyclic variation resulted in smaller corrected angles of attack changes. The corrected angle of attack amplitude was between $A = 1.4°$ and $A = 2.0°$, depending on α_m.

Hysteresis loops were derived for C_L, C_D and C_M from 30 s time series at 100 Hz sample rate. The pitch motion argument, ωt, was divided into 30 bins from 0 to 2π. The aerodynamic loads and α were sorted into these bins and they were averaged at each bin interval. The direction of the hysteresis loops could be found from the development of the hysteresis loop with ωt. The data analysis is described in more detail in Fuglsang *et al.*, 1998 [1].

6.1 $k = 0.11$

A series of seven measurements at different mean angles of attack was taken at $k = 0.11$ with amplitudes between $A = 1.4°$ and $A = 2.0°$.

The individual C_L, C_D and C_M hysteresis loops are shown in Figure 6-1 to Figure 6-3. An arrow under the legend gives the direction of each loop. A right arrow indicates a clockwise loop while a left arrow indicates a counter clockwise loop. In cases of cross over points, the arrow corresponds to the right side part of the loop.

The corresponding stationary flow value curve in the area of each loop is shown for comparison. The stationary flow curves have in the most of the cases a different mean value than the hysteresis loops. This is partly due to the lower sampling rate of the stationary flow measurements and partly due to drifting of the measurement system and uncertainty on the wind tunnel reference. In addition, the influence of the different time lags and the vortex shedding could

also cause a different mean value of the dynamic measurements. However, the slopes and the shapes of the mean curves could be used for comparison.

Figure 6-1 shows the C_L hysteresis loops. In the linear part of the mean C_L curve, the slopes of the hysteresis loops tend to follow the mean curve. The loops are narrow and are counter clockwise.

When the flow starts to separate, the direction of the loops changes to clockwise and they become more open. The slopes of the loops are steeper than the slope of the mean curve. The directions of the loops remain clockwise also in deep stall.
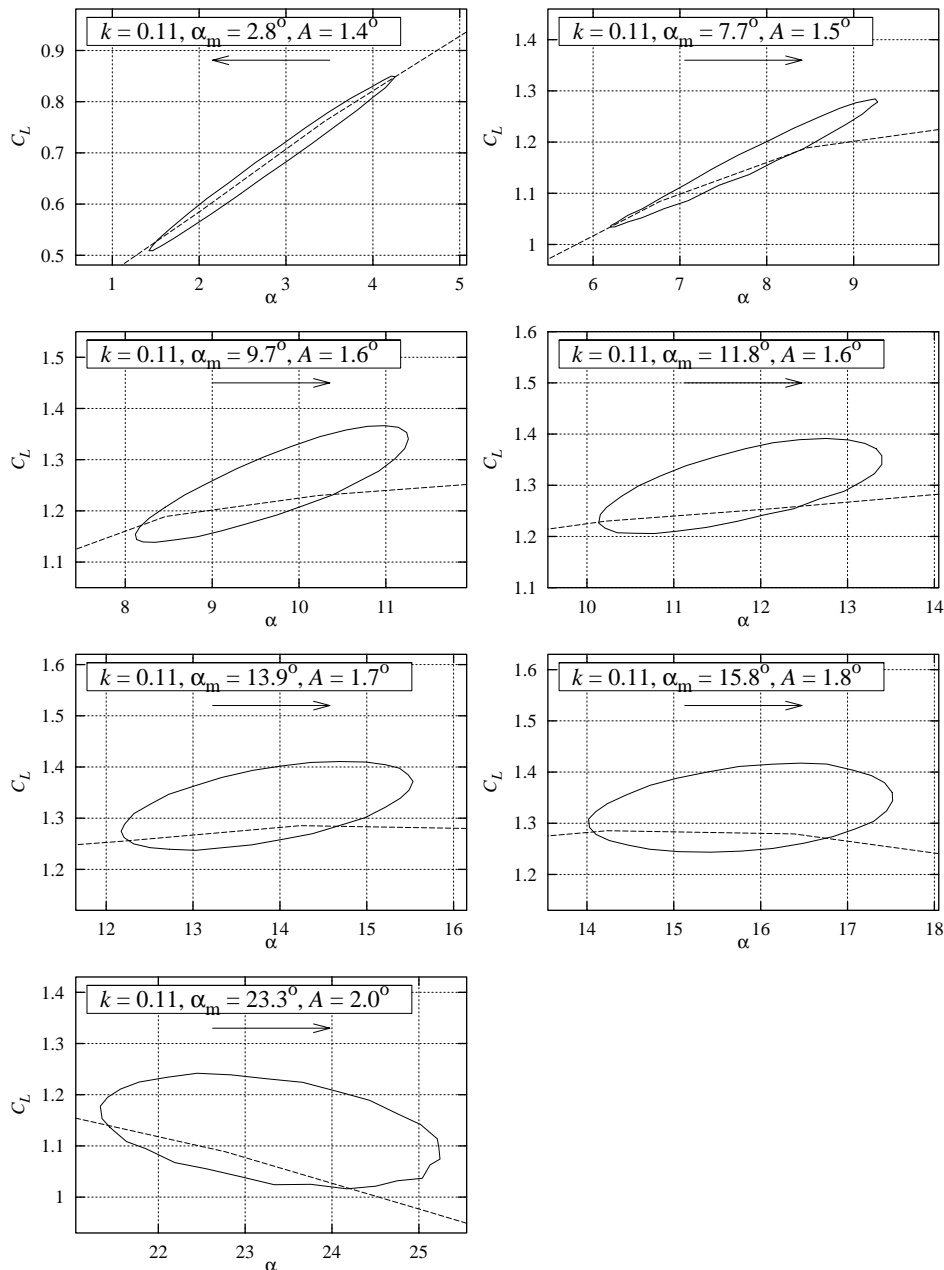

Figure 6-1 Measured C_L hysteresis loops for smooth leading edge flow at k = 0.11, A between 1.4° and 2.0°, Re = 1.6×10^6, (RISØ-1PITCH 221196V1).

Figure 6-2 shows the C_D hysteresis loops. The directions of the loops are clockwise for all measurements. The slopes of the loops tend to follow the slope of the mean curve.
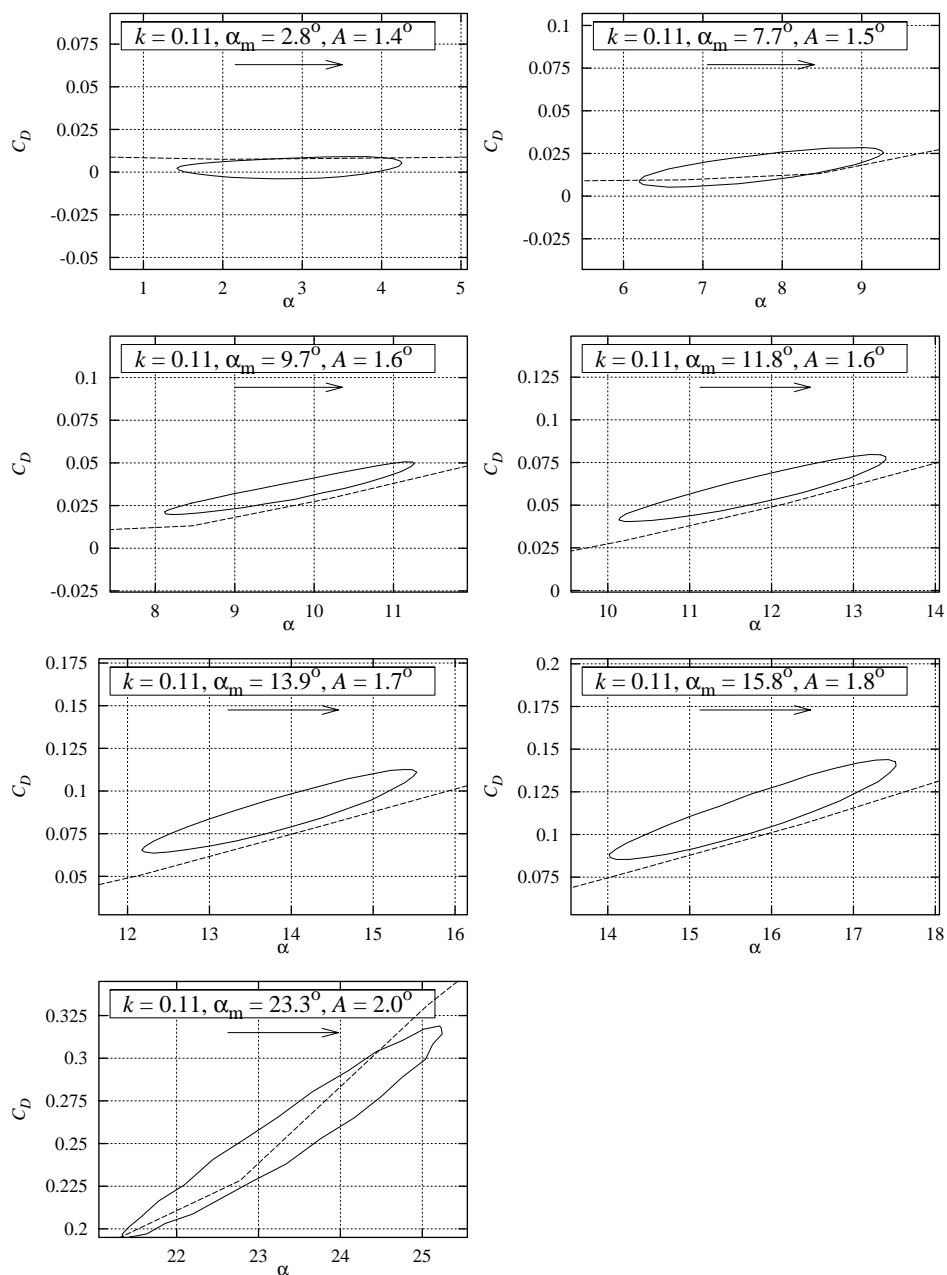

Figure 6-2 Measured C_D hysteresis loops for smooth leading edge flow at k = 0.11, A between 1.4° and 2.0°, Re = 1.6×10⁶, (RISØ-1PITCH 221196V1).

Figure 6-3 shows the C_M hysteresis loops. The directions of the loops are counter clockwise for all measurements and the slopes tend to follow the slope of the mean curve.
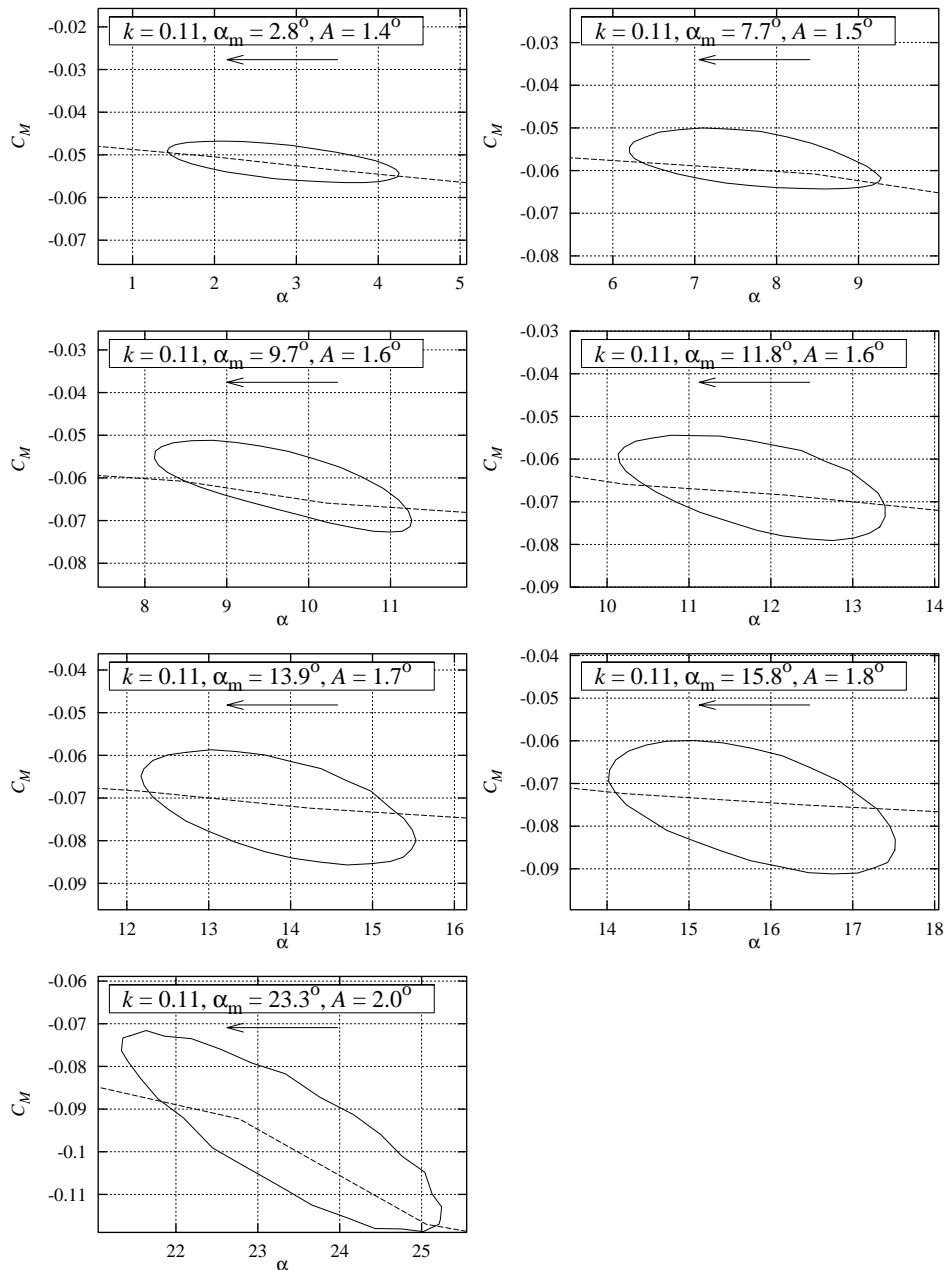

Figure 6-3 Measured C_M hysteresis loops for smooth leading edge flow at k = 0.11, A between 1.4° and 2.0°, Re = 1.6×10⁶, (RISØ-1PITCH 221196V1).

Figure 6-4 shows an overview of the different hysteresis loops compared with the mean curves for C_L, C_D and C_M.
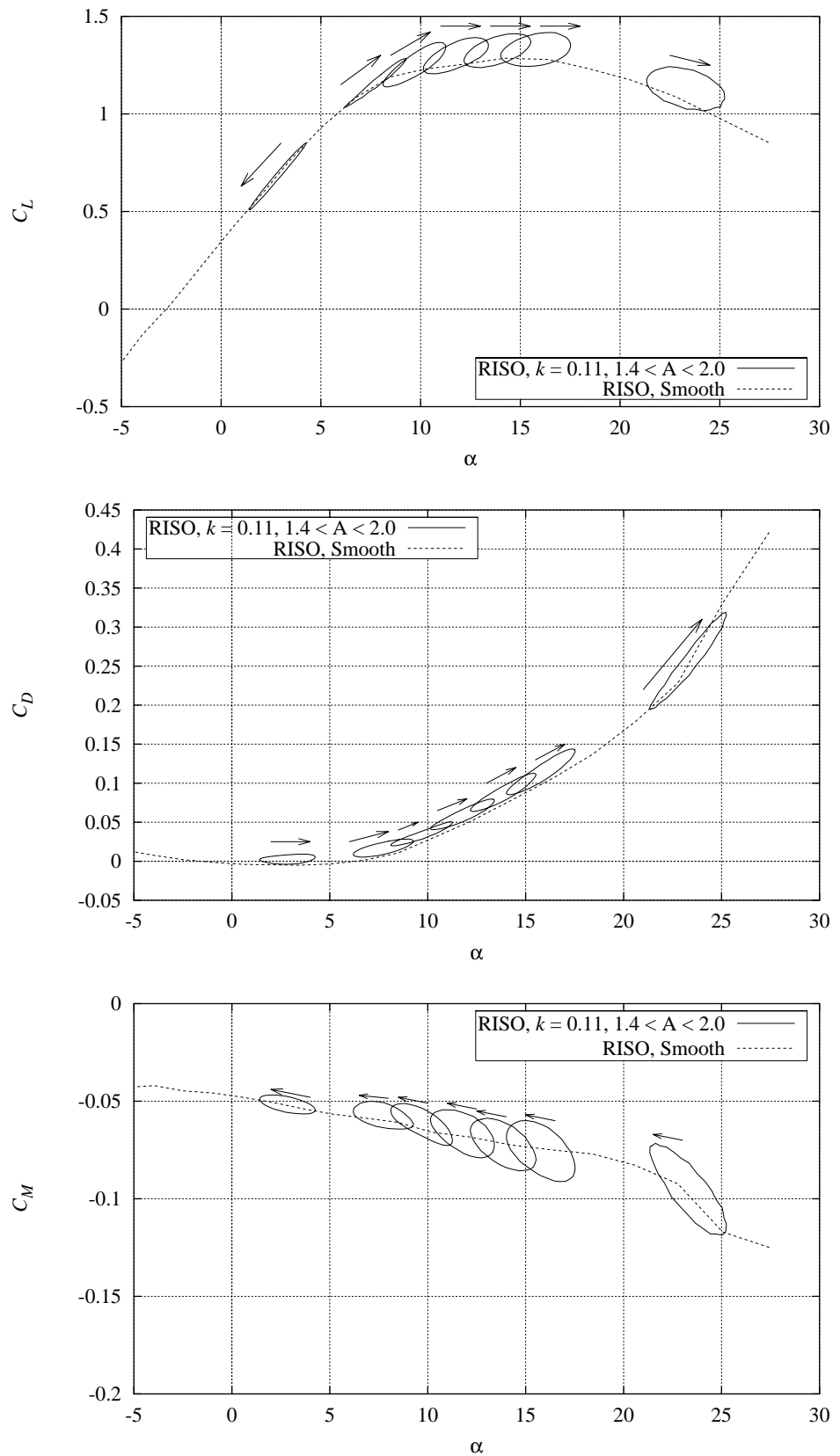
Figure 6-4 Measured C_L, C_D and C_M hysteresis loops compared with mean curves for steady smooth leading edge flow at k = 0.11, A between 1.4° and 2.0°, Re = 1.6×10⁶, (RISØ-1PITCH 221196V1).

6.2 $k = 0.077$

A series of seven measurements at different mean angles of attack was taken at $k = 0.077$ with amplitudes between $A = 1.5°$ and $A = 2.1°$.

The individual C_L, C_D and C_M hysteresis loops are shown in Figure 6-5 to Figure 6-7 and Figure 6-8 shows an overview of the different hysteresis loops compared with the mean curves for C_L, C_D and C_M.

The characteristics of the different hysteresis loops at $k = 0.077$ are identical to the measurements at $k = 0.11$. In general the loops are more narrow for $k = 0.077$ than for $k = 0.11$ and this is caused by the lower reduced frequency.
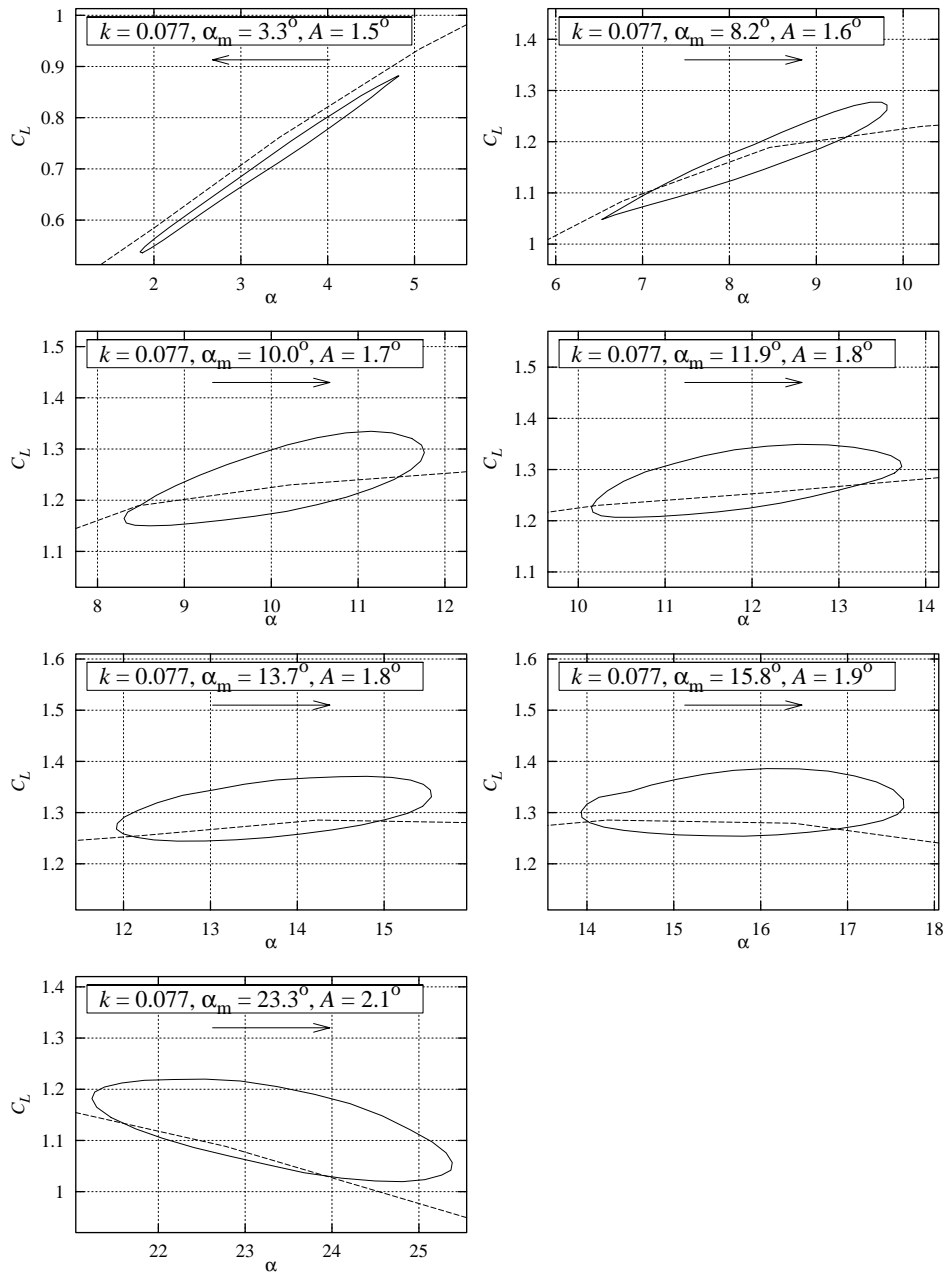

Figure 6-5 Measured C_L hysteresis loops for smooth leading edge flow at $k = 0.077$, A between 1.5° and 2.1°, Re = 1.6×10⁶, (RISØ-1PITCH 221196V2).

The airfoil behaves well and appears to have good dynamic properties. The hysteresis loops are well shaped and they look alike in the entire stall region. They are relatively narrow in stall compared with the NACA 63-215 airfoil, Fuglsang *et al.*, 1998 [1] and the slopes of the C_L hysteresis loops are in general low, which in stall is beneficial to the aerodynamic damping.

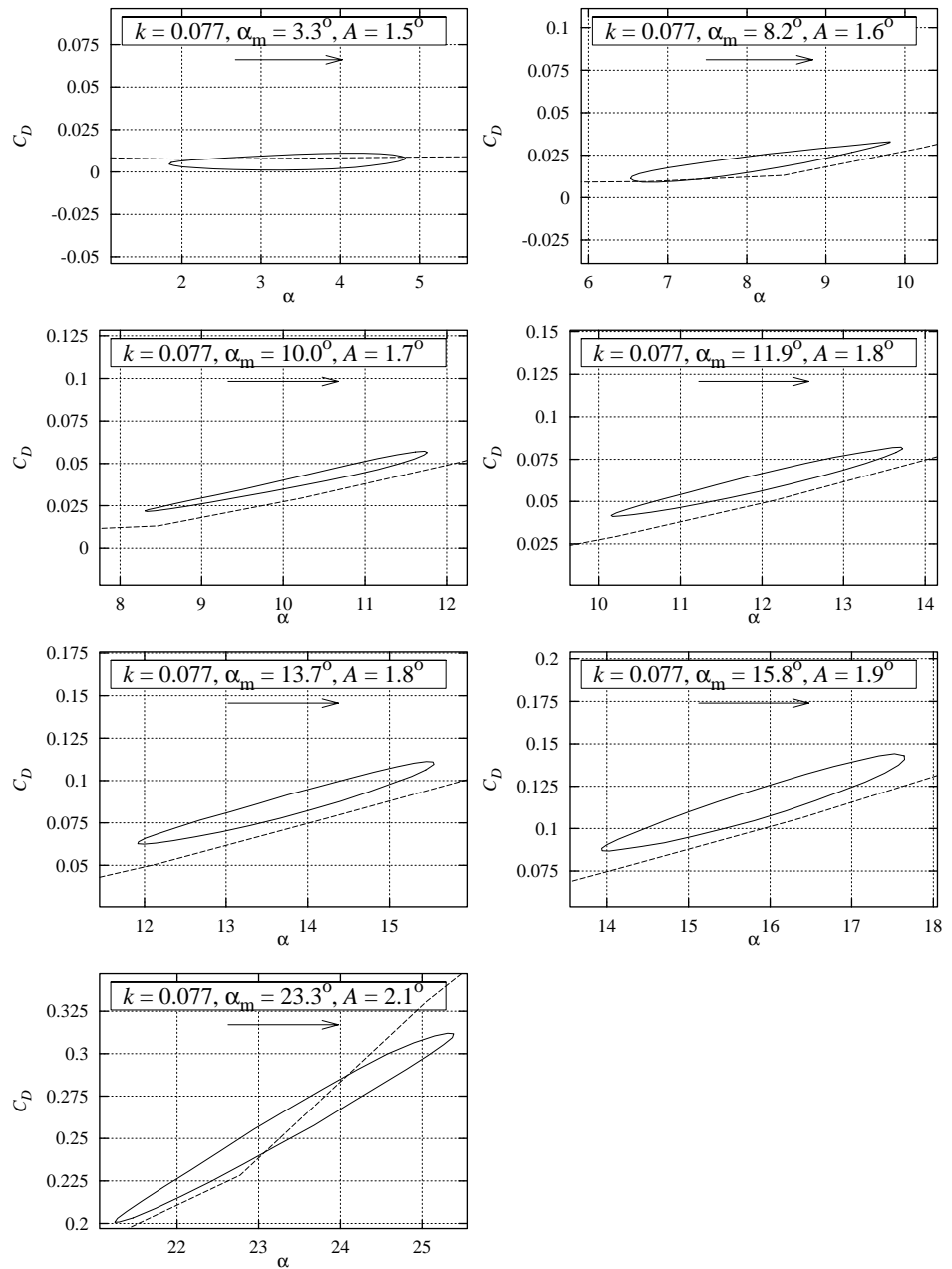*Figure 6-6 Measured C_D hysteresis loops for smooth leading edge flow at k = 0.077, A between 1.5° and 2.1°, Re = 1.6×10^6, (RISØ-1PITCH 221196V2).*

Figure 6-7 Measured C_M hysteresis loops for smooth leading edge flow at k = 0.077, A between 1.5° and 2.1°, Re = 1.6×10⁶, (RISØ-1PITCH 221196V2).

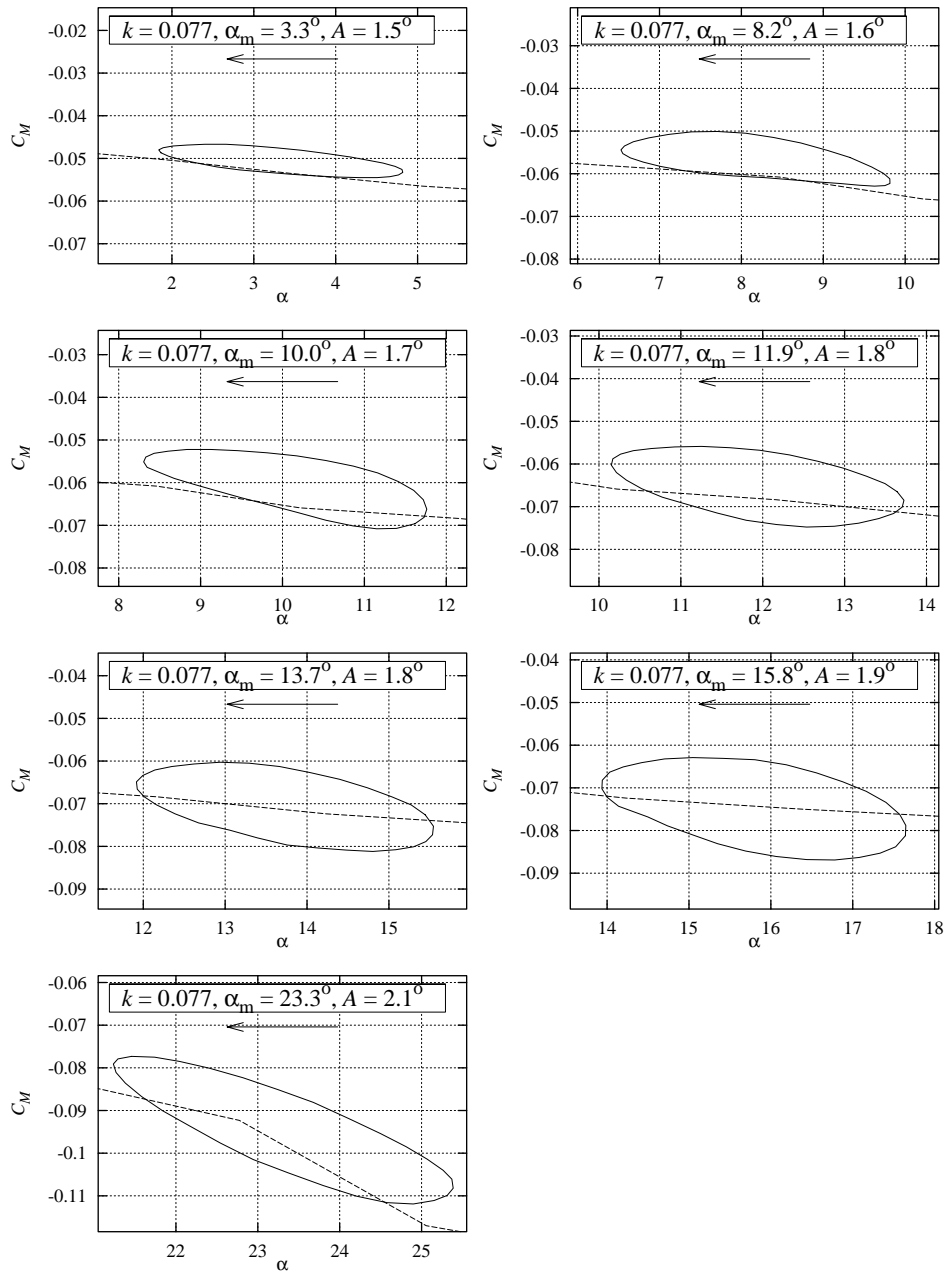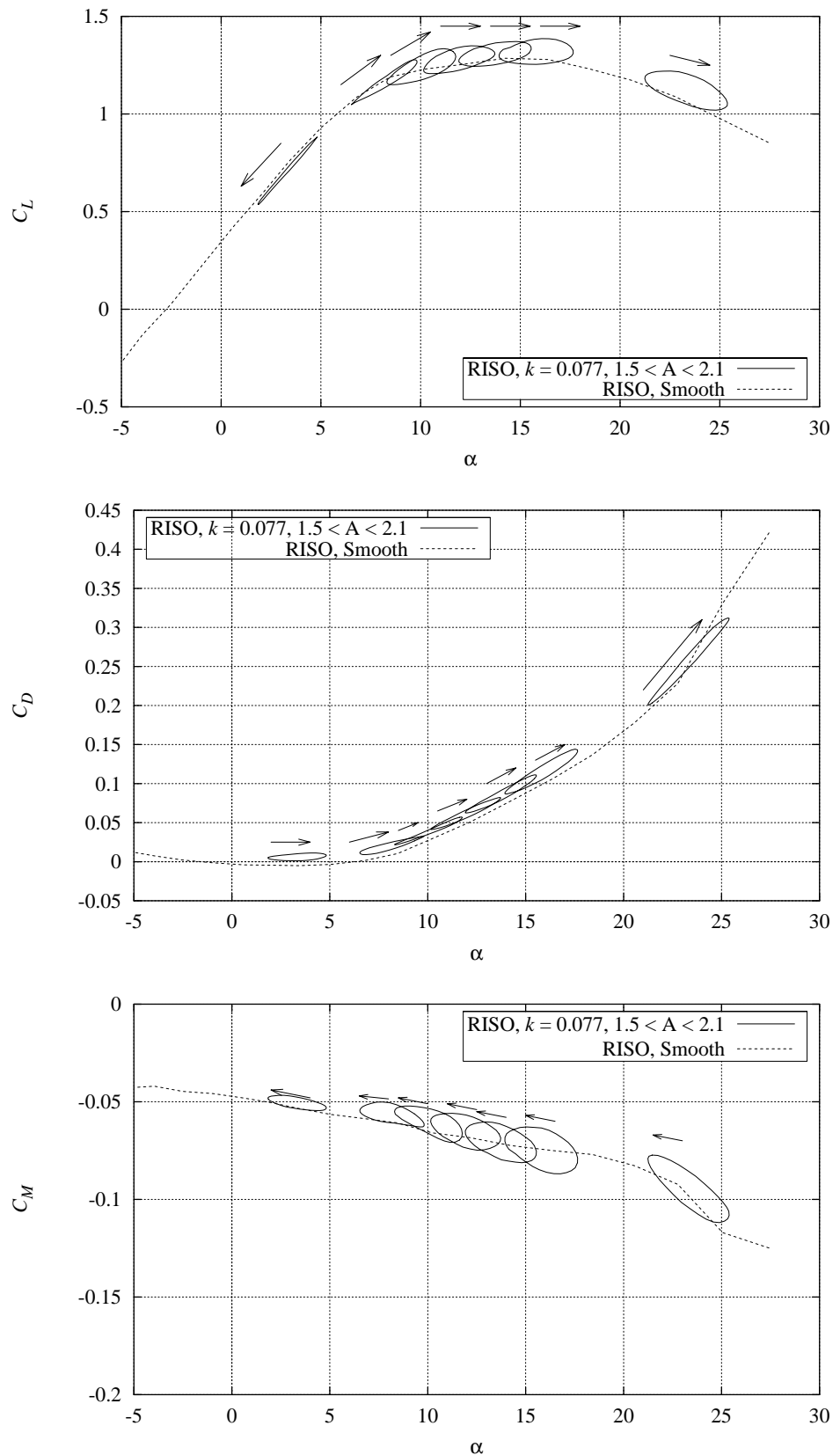*Figure 6-8 Measured C_L, C_D and C_M hysteresis loops compared with mean curves for steady smooth leading edge flow at k = 0.077, A between 1.5° and 2.1°, Re = 1.6×10⁶, (RISØ-1PITCH 221196V2).*

7 Time series

Long duration time series of C_L, C_D and C_M contain information of the stability of the airfoil flow. Especially at high angles of attack in stall, some airfoils are known to suffer from so called 'double stall', Bak *et al.*, 1998 [11] and Fuglsang *et al.*, 1998 [1]. They have very unstable flow patterns with several different C_L levels to apparently identical average inflow conditions.

High frequency steady measurements with 100 Hz sample frequency were taken at low and high angles of attack respectively to see the difference in C_L, C_D and C_M.

Figure 7-1 shows C_L, C_D and C_M respectively for $\alpha = 6.1°$ whereas Figure 7-2 shows C_L, C_D and C_M for $\alpha = 18.3°$. The axis ranges for each aerodynamic load coefficient were chosen identical for best comparison.
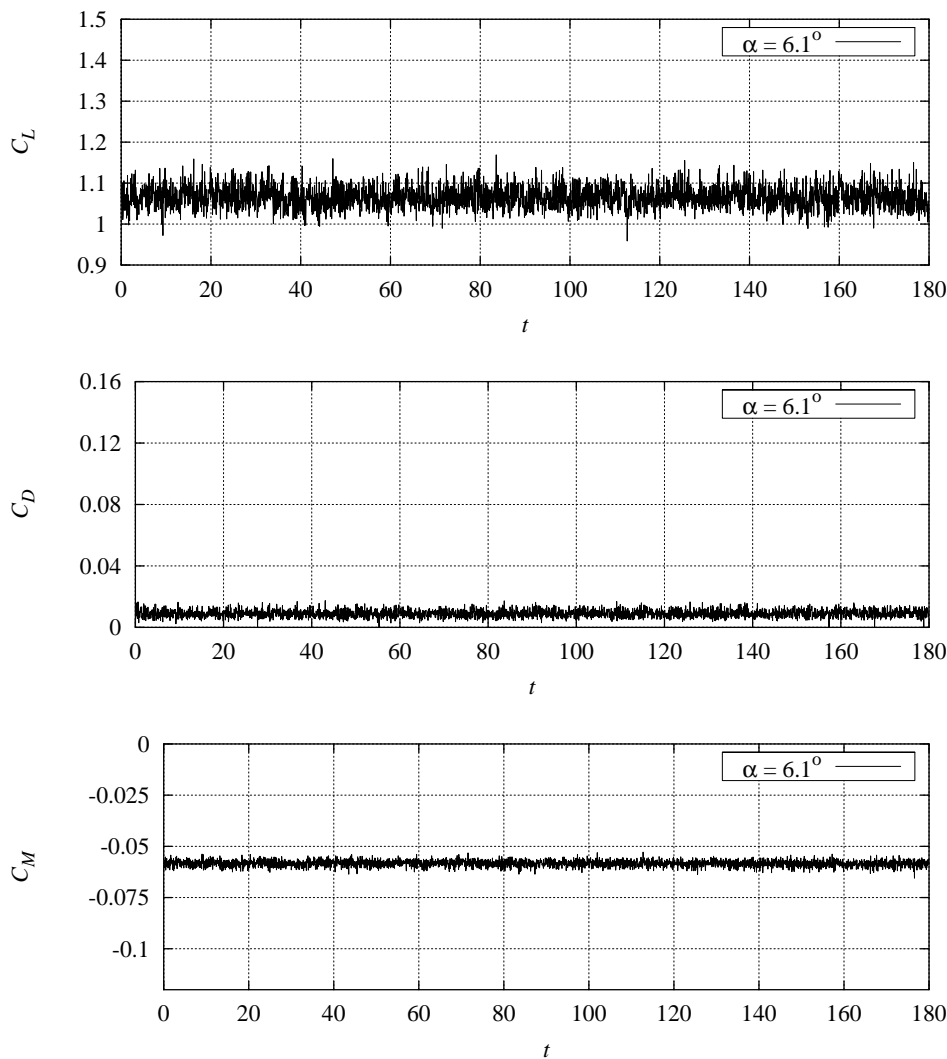
Figure 7-1 Measured C_L, C_D and C_M time series at $\alpha = 6.1°$ (RISØ-1STAT 221196V1).

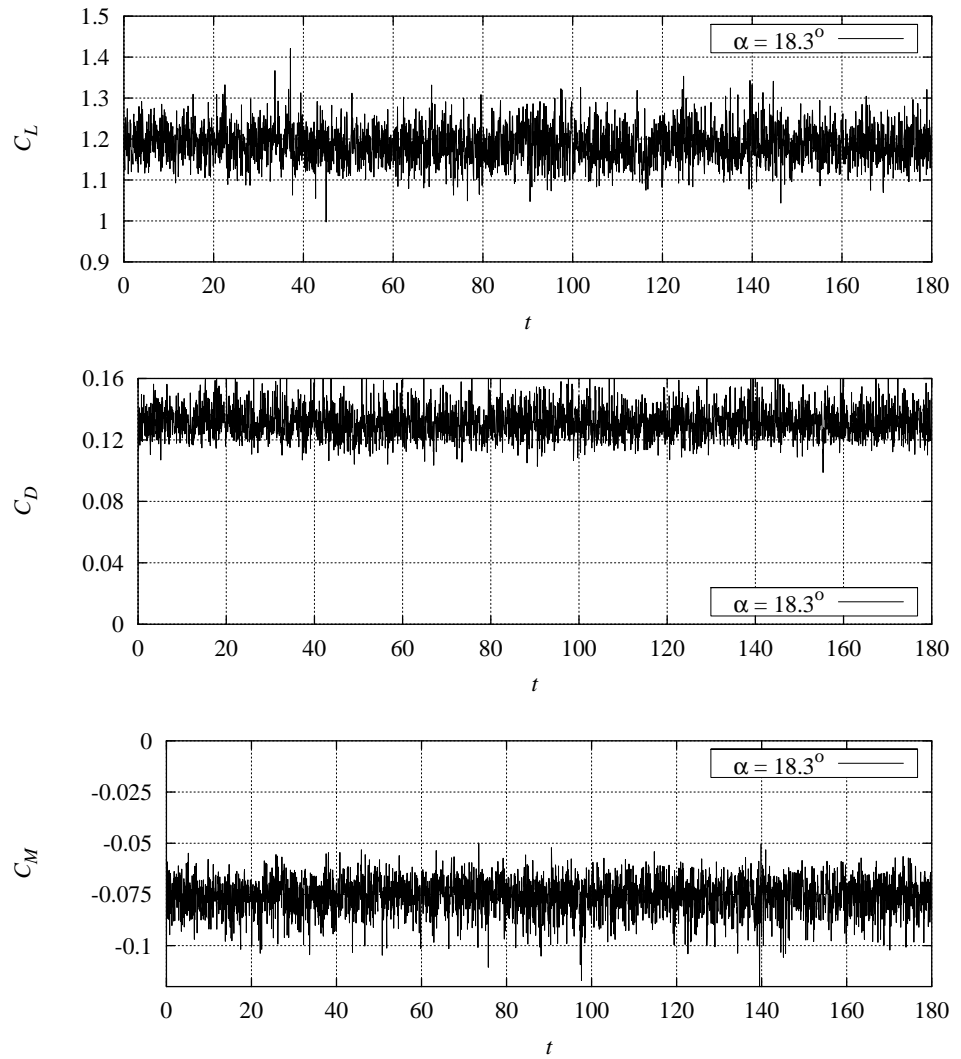*Figure 7-2 Measured C_L, C_D and C_M time series at $\alpha = 18.3°$ (RISØ-1STAT 221196V1).*

For all aerodynamic loads, the standard deviation increases with the angle of attack and especially C_D and C_M are unsteady at high angles of attack. However, the C_L time series show no signs of double stall and in general the flow appears to be stable.

8 Conclusions

Wind tunnel tests with approximately 2d flow were carried out for the RISØ-1 airfoil in the VELUX open jet wind tunnel. The airfoil section was installed in a test stand with endplates on both ends and the test stand was inserted into the tunnel test section. The Reynolds number was 1.6 million and the airfoil had a chord of 0.6 m and a span of 1.9 m. The aerodynamic load coefficients were found from pressure distribution measurements and the total drag coefficient was found from wake rake measurements. Wind tunnel corrections were applied for streamline curvature and down-wash. A proper reference was obtained for normalisation of the aerodynamic load coefficients by use of Pitot measurements at different tunnel locations.

Steady measurements showed that the airfoil behaved well according to the design assumptions with a linear lift curve slope of 0.115 until 8° and a well defined maximum lift coefficient of 1.3 at 14.5°. The stalled region of the lift curve was smooth. The minimum drag was determined to 0.0075.

Comparisons were carried out with the XFOIL viscous/inviscid code and with the EllipSys2D Navier-Stokes code. XFOIL predicted a laminar separation bubble on the suction side at angles of attack from 1° to 8°. Convergence was not stable and the results were not reliable. XFOIL furthermore underestimated minimum drag and overestimated maximum lift. The EllipSys2D code results were in good agreement with the measurements. Minimum drag was well captured and maximum lift was only slightly overestimated.

Leading edge roughness effects were measured to reduce the maximum lift coefficient to 1.1 and to increase the drag coefficient at low incidence. The measured drag curve was in good agreement with predictions. However, the roughness effects on the measured lift curve were too severe compared with the numerical predictions. It was concluded that this was because of the thickness of the applied sand paper. Future measurements should instead use well documented trip tape.

Measurements with the airfoil in pitching motion were carried out to study the hysteresis effects on the aerodynamic coefficients. The reduced frequencies 0.11 and 0.077 with amplitudes 1.4° to 2.1° were measured. The hysteresis loops were regular. The lift coefficient hysteresis loops were counter clockwise at low angles of attack and clockwise in stall and had positive slopes compared with the steady mean curve slopes. All drag coefficient hysteresis loops were clockwise whereas all moment coefficient hysteresis loops were counter clockwise.

Steady inflow measurements at high angles of attack showed that even though the standard deviation on the aerodynamic loads increase with the angle of attack, the airfoil is very steady even in stall. There were no signs of double stall effects.

References

[1]   Fuglsang, P., Antoniou, I., Sørensen, N.N., Madsen, H. Aa., (1998) 'Validation of a Wind Tunnel Testing Facility for Blade Surface Pressure Measurements.' Risø-R-981(EN), Risø National Laboratory, Denmark.

[2]   Madsen, H.A., (1994) 'Design of a 20 kW – 12.6 m stall regulated rotor.' (In Danish) Risø-I-809(DA). Risø National Laboratory, Denmark.

[3]   Antoniou, I., Madsen, H.A., Kretz, A., (1994) 'Testing of a 20 kW – 12.6 m stall regulated rotor.' (In Danish), Risø-I-788(DA). Risø National Laboratory, Denmark.

[4]   Rae Jr., W.H., Pope, A., (1984) 'Low-Speed Wind Tunnel Testing.' SE, John Wiley & Sons, ISBN 0-471-87402-7.

[5]   Brooks, T.F. and Marcolini, M.A., (1984) 'Airfoil Trailing Edge Flow Measurements and Comparison with Theory Incorporating Open Wind Tunnel Corrections.' AIAA-84-2266, AIAA/NASA 9th Aeroacoustic Conference.

[6]   Madsen, H.A., Filippone, A, (1995) 'Implementation and Test of the XFOIL Code for Airfoil Analysis and Design.' Risø-R-644(EN), Risø National Laboratory, Denmark.

[7]   Drela, M., (1989) 'XFOIL: An Analysis and Design system for Low Reynolds Number Airfoils, In: Low Reynolds Number Aerodynamics.' Springer-Verlag Lec. Notes in Eng. 54.

[8]   Sørensen, N.N., (1995) 'General Purpose Flow Solver Applied to Flow over Hills.' Risø-R-827(EN), Risø National Laboratory, Denmark.

[9]   Menter, F.R., (1993) 'Zonal Two Equation k-ω Turbulence Models for Aerodynamic Flows.' AIAA Paper 93-2906.

[10] Michel, R., (1952) 'Etude de la transition sur les profiles d'aile. ONERA Report 1/1578-A.' See White F.M., Viscous fluid flow, p. 442.

[11] Bak, C.; Madsen, H.A.; Fuglsang, P.; Rasmussen, F., (1998) 'Double Stall.' Risø-R-1043(EN), Risø National Laboratory, Denmark.

A1 Measurement survey

This appendix describes the performed measurements in detail to support the understanding of the discussed measurements in the report and for use in subsequent exploitation. The different measurement types are described and the naming convention for the data files is explained. The format of the data files is given and each performed measurement is listed and described.

A1.1   Measurement types

There are four different basic types of measurements of the airfoil flow as shown in Table A1-1.

Table A1-1 Overview of the different types of measurements that have been performed.

Name	Short description	Purpose
STEP	• Discrete measurements at different angles of attack. • Angle of attack range: -6° to 30°. • Interval between different angles: 1° to 4°. • Time series length: 20 s. • Sampling frequency: 5 Hz.	The steady C_L, C_D and C_M polar.
CONT	• Continuos measurements at different angles of attack. • Angle of attack range: -6° to 30°. • Rate of change of angle of attack: 0.1°/s to 0.5°/s (manually changed). • Time series length app: 250 s. • Sampling frequency: 50 Hz.	The quasi steady C_L, C_D and C_M polar.
STAT	• Stationary measurements at different angles of attack. • Time series length: 20s to 180s. • Sampling frequency: 100 Hz.	Time series of airfoil flow at different angles of attack, usually in stall.
PITCH	• Dynamic measurements at different mean angles of attack with the airfoil in pitching motion. • Pitching amplitude: 2° to 5° • Reduced frequency: until 0.12 • Time series length: 30s to 40s. • Sampling frequency: 100 Hz.	Time series of unsteady airfoil flow from pitching motion for determination of hysteresis loops for C_L, C_D and C_M at different mean angles of attack, pitching amplitudes and pitching frequencies.

A1.2 Data file naming convention

The different data files are named by:
- The name of the airfoil.
- The measurement type keyword from Table A1-1.
- The date of measurement, data, DD, month, MM, year, YY, 'DDMMYY'.
- A version number, VNN, where NN is the version number.
- The filename extension. For time averaged data, '.DAT', and for time series, 'NNN', where NNN is a time series run number.

An example is shown in Table A1-2.

Table A1-2 Example of naming convention of data files

RISO-1	STEP	2221196	V1	.DAT

A1.3 Data file format

The format of the data files is described in Table A1-3. Each measurement frame/average is written formatted subsequently in rows.

Table A1-3 The content of the columns in the data files.

Col.	Symbol	Sensor	Unit	Description
1	α_c	αc	°	Corrected angle of attack
2	C_L	cl	-	Lift coefficient (pressure)
3	C_{Dc}	cdc	-	Corrected drag coefficient (wake rake + pressure)
4	C_{Mc}	cmc	-	Corrected moment coefficient (pressure)
5	C_{Dpc}	cdpc	-	Corrected drag coefficient (pressure)
6	C_{Dw}	cdw		Drag coefficient (wake rake)
7	α	α	°	Raw angle of attack
8	C_D	cd	-	Raw drag coefficient (wake rake + pressure)
9	C_{Dp}	cdp		Raw drag coefficient (pressure)
10	C_M	cm	-	Raw moment coefficient (pressure)
11	Re	re		Free stream Reynolds Number
12	q_∞	qref	Pa	Free stream dynamic pressure
13	p_∞	ps,ref	Pa	Free stream static pressure
14	T	t	°	Tunnel temperature
15	p_{atm}	patm	mBar	Atmospheric pressure
16-72	C_P	cp(x)		Pressure coefficients corresponding to the coordinates in top row
72-74	p_{1-3}	ps,Pitot()	Pa	Pitot tube static pressures
75-77	p_{o1-3}	pt,Pitot()	Pa	Pitot tube total pressures
78-82	p_w	ps,wake	Pa	Wake rake static pressures corresponding to the coordinates in top row
83-131	p_{ow}	pt,wake	Pa	Wake rake total pressures corresponding to the coordinates in top row

A1.4   Performed measurements

Table A1-4 contains a list of the performed measurements.

Table A1-4 Performed measurements

Data file	Extension	Description and remarks
RISO-1 STEP 221196 V1	001-037	• Smooth leading edge • 20s time series at 5 Hz for each α
	DAT	• 20s average values
RISO-1 CONT 221196 V1	DAT	• Smooth leading edge • 50 Hz time series at different α
RISO-1 CONT 221196 V2	DAT	• Leading edge roughness, sand paper • 50 Hz time series at different α
RISO-1 STAT 221196 V1	000-005	• Smooth leading edge • 180s time series at 100 Hz for constant α
RISO-1 STAT 221196 V1	006-007	• Smooth leading edge • The clearance between the airfoil span and the endplates was sealed with tape to promote 2d flow • 180s time series at 100 Hz for constant α
RISO-1 PITCH 221196 V1	000-006	• Smooth leading edge • Amplitude between $1.4° < A < 2.0°$ • Reduced frequency, $k = 0.11$ • 30 s time series at 100 Hz for each α
RISO-1 PITCH 221196 V2	000-006	• Smooth leading edge • Amplitude between $1.5° < A < 2.1°$ • Reduced frequency, $k = 0.077$ • 30 s time series at 100 Hz for each α

Bibliographic Data Sheet

Risø-R-999(EN)

Abstract (max. 2000 characters)

Wind tunnel tests with approximately 2d flow were carried out for the RISØ-1 airfoil in the VELUX open jet wind tunnel. The airfoil section was mounted in a test stand equipped with end plates to retain 2d flow conditions. The stand was then inserted into the tunnel test section. The Reynolds number was 1.6 million, the chord of the airfoil model 0.6 m and the span 1.9 m. Pressure distribution measurements provided the aerodynamic load coefficients and wake rake pressure measurements provided the total drag coefficient. Wind tunnel corrections were applied for streamline curvature and down-wash. Steady inflow measurements showed that the airfoil behaved well with a well defined maximum lift coefficient of 1.3, a minimum drag of 0.0075, and a smooth stall region. Comparisons with numerical predictions from the EllipSys2D Navier-Stokes code showed good agreement among the calculated and measured lift and drag coefficients. Leading edge roughness devices were found to reduce the maximum lift coefficient by 15% to 1.1 and to increase the drag coefficient at low incidence. Dynamic inflow measurements with the airfoil in pitching motion were carried out to study the hysteresis effects on the aerodynamic coefficients. The lift coefficient hysteresis loops at high incidence had smooth shapes and did not show leading edge separation. Steady inflow measurements at high angles of attack showed that the airfoil flow was stationary and did not indicate double stall.